

## Fragment-Molecular-Orbital-Method-Based *ab Initio* NMR Chemical-Shift Calculations for Large Molecular Systems

Qi Gao,<sup>†,‡</sup> Satoshi Yokojima,<sup>\*,†,¶</sup> Dmitri G. Fedorov,<sup>§</sup> Kazuo Kitaura,<sup>§,||</sup>  
Minoru Sakurai,<sup>‡</sup> and Shinichiro Nakamura<sup>\*,†,‡,¶</sup>

Mitsubishi Chemical Group Science and Technology Research Center, Inc., 1000  
Kamochida-cho, Aoba-ku, Yokohama 227-8502, Japan, Center for Biological Resources  
and Informatics, Tokyo Institute of Technology, 4259 Nagatsuda-cho, Midori-ku, Yokohama  
226-8501, Japan, The KAITEKI Institute, Inc. 14-1, Shiba 4-chome, Minato-ku, Tokyo  
108-0014, Japan, RICS, National Institute of Advanced Industrial Science and Technology  
(AIST), 1-1-1 Umezono, Tsukuba, Ibaraki 305-8568, Japan, and Graduate School of  
Pharmaceutical Sciences, Kyoto University, Sakyo-ku, Kyoto 606-8501, Japan

Received October 6, 2009

**Abstract:** An *ab initio* computational method, based on the fragment molecular orbital (FMO) method, for calculating nuclear magnetic resonance (NMR) chemical shifts has been developed by introducing the concept of a merged fragment with a cutoff distance. Using point charges or density based on electrostatic potential obtained from FMO calculations, the NMR calculations (GIAO and CSGT) with the 6-31G(d) and 6-311G(d,p) basis sets were performed on  $\alpha$ -helix and  $\beta$ -sheet polypeptides. The cutoff distance defines the optimal merged fragment size for NMR calculations. This method accurately reproduces electrostatic effects and magnetic susceptibilities. The chemical shifts determined with a cutoff distance not shorter than 8 Å for both  $\alpha$ -helix and  $\beta$ -sheet polypeptides agree well with those calculated by conventional *ab initio* NMR calculations.

### 1. Introduction

In the fields of chemical and biological research, nuclear magnetic resonance (NMR) spectroscopy is one of the most valuable experimental methods for determining chemical and structural properties. Since NMR chemical shifts are very sensitive to changes in the molecular structure, they are widely used for monitoring the surrounding environment of individual atoms. However, in the case of large biological

molecules, the process of obtaining the required signal-to-noise ratio (SNR) when measuring NMR spectra is time-consuming.

Several theoretical methods for computing NMR chemical shifts of *small* organic molecules have been established. These methods can be divided into two primary categories. The first are *ab initio* methods dealing with gauge-dependence problems such as the “gauge-including atomic orbital” (GIAO)<sup>1,2</sup> and the “continuous set of gauge transformations” (CSGT).<sup>3</sup> Those methods can reliably be applied to structures of organic and inorganic compounds using appropriate basis sets. However, when it comes to large molecules such as proteins, the computational cost becomes quite large, so not so many applications of *ab initio* methods have been reported.<sup>4</sup> The second category is empirical methods that predict NMR chemical shifts in a very short time using a large database. Nonetheless, because these methods have not been parametrized to reproduce NMR chemical shifts of an arbitrary molecule, they fail to predict chemical shifts of some new specific compounds.

\* To whom corresponding should be addressed. Tel: +81-45-963-3833 (S.Y.), +81-45-963-3265 (S.N.). Fax: +81-45-963-3835 (S.Y.), +81-45-963-3835 (S.N.). E-mail: yokojima@rsi.co.jp (S.Y.), shindon@rsi.co.jp (S.N.).

† Mitsubishi Chemical Group Science and Technology Research Center, Inc.

¶ The KAITEKI Institute, Inc.

‡ Tokyo Institute of Technology.

§ AIST.

|| Kyoto University.

The hybrid quantum-mechanical/molecular-mechanical (QM/MM) method<sup>5,6</sup> is a computational tool that can be used to predict the NMR chemical shifts in large molecules. In the QM/MM method, a part for calculating NMR chemical shifts is described with QM methods, whereas the remaining part is described with MM methods. Cui and Karplus proposed a method for calculating chemical shifts using the GIAO in the QM/MM framework.<sup>7</sup> After carefully comparing the results of the QM/MM model to those of full QM calculations, they concluded that the former can provide good descriptions of environmental effects on chemical shifts. The error compared to full QM calculations is 1–2 ppm for heavy atoms when the distance between the atom of interest in the QM part and the MM part is more than 2.5 Å. The importance of the contributions of the Pauli repulsion and magnetic susceptibility is also evident from their studies. If these contributions are neglected at distances of less than 2.5 Å,<sup>7</sup> large errors occur. Similar results have also been reported by Ishida,<sup>8</sup> He et al.,<sup>9</sup> and Sebastiani et al.<sup>10–12</sup> For example, Sebastiani and Rothlisberger<sup>10,11</sup> have modified the standard QM/MM interaction potential by including the Pauli repulsion explicitly in the QM/MM interaction potential. They concluded that the modified QM/MM interaction potential can reproduce full QM results.

In contrast with these QM/MM NMR studies in which the interactions between QM and MM regions have been handled as described by Field et al.,<sup>13</sup> a study by Gascón et al.<sup>14,15</sup> used the ONIOM<sup>16</sup> electronic-embedding method to calculate the NMR data of large molecules, and their calculation results agreed well with experimental measurements. Hall et al.<sup>17</sup> have recently used a three-layer ONIOM (B3LYP:HF:AMBER) scheme to calculate the NMR chemical shifts of the retinal chromophore in rhodopsin.

In addition to the partial quantum-mechanical description, there are some fragment-based methods where the whole system is described quantum mechanically.<sup>18–25</sup> The fragment molecular orbital (FMO) method<sup>26–31</sup> is one of such fragment-based methods applied to *ab initio* calculations<sup>32–36</sup> of large molecules. Sekino et al.<sup>37</sup> have developed the FMO2-NMR method, where the FMO many-body expansion has been applied to the computation of chemical shifts.

We recently developed an *ab initio* method<sup>38</sup> based on FMO1 for computing the NMR response in protein systems. This method involves inexpensive single-fragment NMR calculations including the electrostatic effects from other fragments. Our method<sup>38</sup> of computing NMR chemical shifts consists of two parts. First, a molecular system is divided into various fragments, and the electron densities of these fragments are obtained by carrying out FMO calculations. Second, for the neighboring dimer fragments in the electrostatic potential (ESP) of other fragments, nuclear magnetic shielding constants are computed with GIAO and/or CSGT methods. Here, the chemical shift,  $\delta$ , is related to the nuclear magnetic shielding tensor,  $\sigma$ , by a reference standard,  $\sigma^0$ , as<sup>39</sup>  $\delta = (\sigma^0 - \sigma^{\text{iso}})/(1 - \sigma^0) \times 10^6 \approx (\sigma^0 - \sigma^{\text{iso}}) \times 10^6$ , where the absolute isotropic shielding constant,  $\sigma^{\text{iso}} = \text{Tr}(\sigma)/3$ .

Although this method can reasonably reproduce experimental and conventional *ab initio* calculated chemical shifts,

errors of 2 ppm for <sup>13</sup>C, 4.5 ppm for <sup>15</sup>N, and 0.8 ppm for <sup>1</sup>H are still larger than the desired level, namely, below 0.5 ppm for heavy atoms and 0.1 ppm for hydrogen atoms.<sup>38</sup> Furthermore, these calculations have been less accurate in predicting anisotropic shielding constants.<sup>38</sup> We previously used our method<sup>38</sup> to calculate chemical shifts of a  $\beta$  sheet.<sup>40</sup> However, the errors were even larger than those stated above because of a lack of accuracy in reproducing the electrostatic effects and magnetic susceptibilities.

Previous quantum chemical and experimental studies<sup>41–44</sup> on NMR chemical shifts in various chemical environments have indicated that the electrostatic effect and magnetic susceptibility arise not only from covalent-bond interactions but also from weaker interactions such as hydrogen bonds, the susceptibility of conjugated carbon groups, and the polarization of the surrounding environment. These studies have emphasized that, to accurately reproduce the electron distributions around atoms, the inclusion of these interactions is crucial.

Other sources of error due to our method<sup>38</sup> may arise from border atoms, i.e., atoms on the border of two fragments. We have analyzed the influence of border atoms on the ESP around them. When the positions of border atoms are far enough away from the atom of interest, our method<sup>38</sup> reproduced the ESP of the conventional *ab initio* method. However, when these distances are shorter, the method yields relatively inaccurate ESP, resulting in large errors in chemical shifts.

The purpose of the present study was to develop a new method—using a new cutoff-distance-based fragmentation scheme—that can accurately reproduce conventional *ab initio* isotropic and anisotropic shielding constants. This method adopts the effective framework of the FMO1 method, which is conceptually similar to the multilayer structure of QM/MM. Unlike the QM/MM method, the effect of the MM part is described by the ESP derived from quantum mechanics. The main difference of the cutoff-distance-based method from our previous method for computing nuclear magnetic shielding constants from the electronic structure of neighboring dimer fragments<sup>38</sup> is that a cutoff distance to define the size of merged fragments is introduced to calculate nuclear magnetic shielding constants. The density matrix of a merged fragment describes the electrostatic response better than that of a dimer fragment. In addition, the cumbersome use of the two fragmentation schemes in our previous method is eliminated. Using the cutoff-distance-based method, we assessed the dependence of nuclear magnetic shielding constants on cutoff distance, basis sets, and polypeptide structures. Excellent agreement between the shielding constants of the cutoff-distance-based method with those of the conventional *ab initio* method is attained when the cutoff distance is  $\geq 8$  Å. The isotropic shielding constants of all the tested heavy atoms (<sup>13</sup>C and <sup>15</sup>N) and <sup>1</sup>H atoms obtained by the cutoff-distance-based method with a cutoff distance of 8 Å reproduce the values obtained with the conventional *ab initio* method (CSGT) within 0.24 ppm and 0.11 ppm, respectively.

## 2. Theory

**2.1. FMO Method.** The FMO method<sup>28,45</sup> developed by Kitaura et al. is designed to calculate the electronic state of large systems within the *ab initio* framework. First, a large system is divided into  $N$  fragments (monomers). The total energy is then given by

$$E = \sum_I^N E_I + \sum_{I>J} (E_{IJ} - E_I - E_J) \quad (1)$$

where energy  $E_I$  of monomer  $I$  and energy  $E_{IJ}$  of dimer  $IJ$  (a pair of monomers  $I$  and  $J$ ) are summed. At the RHF level, the contributions of the monomer and dimer to the total energy can be calculated by

$$\tilde{\mathbf{F}}^x \mathbf{C}^x = \mathbf{S}^x \mathbf{C}^x \tilde{\boldsymbol{\epsilon}}^x \quad (2)$$

$$\tilde{\mathbf{F}}^x = \tilde{\mathbf{H}}^x + \mathbf{G}^x \quad (3)$$

$$\tilde{H}_{\mu\nu}^x = H_{\mu\nu}^x + V_{\mu\nu}^x + \gamma \sum_{i \in x} P_{\mu\nu}^i \quad (4)$$

$$P_{\mu\nu}^i = \langle \mu | \varphi_i^h \rangle \langle \varphi_i^h | \nu \rangle \quad (5)$$

$$V_{\mu\nu}^x = \sum_{K \neq x} \left\{ \sum_{A \in K} \left\langle \mu \left| -\frac{1}{4\pi\epsilon_0} \frac{Z_A e^2}{|\mathbf{r} - \mathbf{R}_A|} \right| \nu \right\rangle + \sum_{\rho\sigma \in K} D_{\rho\sigma}^K (\mu\nu | \rho\sigma) \right\} \quad (6)$$

$$(\mu\nu | \rho\sigma) = \frac{e^2}{4\pi\epsilon_0} \int d\mathbf{r}_1 d\mathbf{r}_2 \chi_\mu(\mathbf{r}_1) \chi_\nu(\mathbf{r}_1) |\mathbf{r}_1 - \mathbf{r}_2|^{-1} \chi_\rho(\mathbf{r}_2) \chi_\sigma(\mathbf{r}_2) \quad (7)$$

$$E_x = \frac{1}{2} \text{Tr}\{\mathbf{D}^x (\tilde{\mathbf{H}}^x + \tilde{\mathbf{F}}^x)\} + E_{\text{Nuc}}^x \quad (8)$$

where superscript  $x$  represents a monomer ( $x = I$ ) or a dimer ( $x = IJ$ );  $\mu$ ,  $\nu$ ,  $\rho$ , and  $\sigma$  denote atomic orbitals;  $Z_A$  and  $\mathbf{R}_A$  correspond to the charge and the position of atom  $A$ ; and  $\mathbf{D}^K$  is the density matrix of fragment  $K$ . The Fock matrix,  $\tilde{\mathbf{F}}^x$ , consists of the sum of one-electron term  $\tilde{H}_{\mu\nu}^x$  and two-electron term  $\mathbf{G}^x$ . Note that, in addition to the conventional one-electron term ( $H_{\mu\nu}^x$  in eq 4), there are two more terms on the right-hand side of eq 4, i.e., the ESP  $V_{\mu\nu}^x$  arising from other fragment  $K$  and the orbital projection operator,  $P_{\mu\nu}^i$ , which is made up of hybridized orbital  $\varphi_i^h$  with  $\gamma = 10^6$  hartree for all orbitals.<sup>26</sup>

Prior to the FMO calculations, the fragment borders are first defined appropriately.<sup>45</sup> The ESP is then obtained by iteratively solving the Fock equation of each monomer (eq 2 with  $x = I$ ) until the energy of the monomers with the ESP of other fragments converge. Finally, every dimer (eq 2,  $x = IJ$ ) is calculated once by using the ESP (eq 6 with  $x = IJ$ ) obtained by the previous monomer FMO calculations. In the case of a polypeptide, a two-body expansion with a two residues per fragment division is a reasonable compromise between the attained accuracy and the computational cost incurred.<sup>45</sup> The FMO method has been widely used to

study interactions such as dipole–dipole and  $\pi$ – $\pi$  interactions in biomolecular systems.<sup>32,33,46</sup>

**2.2. GIAO and CSGT Methods.** Chemical shifts can be evaluated theoretically by adding the contribution of the external magnetic field described by a vector potential to a Hamiltonian. Doing so, however, faces a new problem. Because the size of a basis set is finite, the calculated chemical shifts depend on the location of the gauge origin of the vector potential. To find a numerical solution to the nuclear magnetic shielding tensor which does not depend on the choice of the gauge origin, two methods have been established, i.e., GIAO<sup>1,2</sup> and CSGT.<sup>3</sup> With the GIAO method, the nuclear magnetic shielding tensor  $\sigma_{\alpha\beta}$  is calculated from eq 9 as the mixed partial derivative of energy  $E$  with respect to external magnetic field  $\mathbf{B}$  and nuclear magnetic moment  $\boldsymbol{\mu}$ . The dependence of the gauge origin is mostly eliminated by using field-dependent atomic orbitals.

$$\sigma_{\alpha\beta} = \frac{\partial^2 E}{\partial \mu_\alpha \partial B_\beta} \quad (9)$$

In the CSGT method,  $\mathbf{J}^{(1)}(\mathbf{r})$ , the linear response of the current density induced by the external magnetic field  $\mathbf{B}$  at the position  $\mathbf{r}$  is determined using  $\mathbf{r}$  as the gauge origin. The shielding at the nuclear position  $\mathbf{r}_N$  is obtained by integrating the magnetic field (induction) generated by the induced current at  $\mathbf{r}_N$  (eq 10).

$$\sigma_{\alpha\beta}(\mathbf{r}_N) = -\frac{\mu_0}{4\pi} \int d^3 r \left[ \frac{\partial \mathbf{J}^{(1)}(\mathbf{r})}{\partial B_\beta} \times \frac{\mathbf{r}_N - \mathbf{r}}{|\mathbf{r}_N - \mathbf{r}|^3} \right]_\alpha \quad (10)$$

**2.3. NMR Computational Models.** In a previous work, by combining the FMO method with either the GIAO or CSGT method, we developed two computational models for calculating the nuclear magnetic shielding tensor of large biomolecular systems, namely, model I and model II.<sup>38</sup> For both models, the Fock matrices of the monomers are calculated using the ESP of other fragments for close fragments within about 5 Å; otherwise, point charges are used. The two models differ in regard to the calculation of the Fock matrices of the dimers which are used to calculate chemical shifts. In model I, the dimer shielding tensors are calculated using a point charge ESP; that is, the point charge ESP from other fragments is constructed from the density matrix of monomers (Mulliken charges). Model II uses the ESP of other fragments without approximation. Fock matrices of dimers that are built on neighboring monomer pairs along the sequence of a given polypeptide are calculated by solving eq 2 for dimer  $IJ$  (usually,  $|I - J| = 1$ ). CPHF equations are then directly solved by using the Fock matrix to obtain the shielding tensor of the atoms in the dimer. GIAO is used in model I, whereas CSGT is used in both models I and II.<sup>38</sup>

Our previous tests<sup>38</sup> established that models I and II could reproduce the conventional quantum-chemical isotropic-shielding constants fairly well. Although model I could be applied to very large molecules, it created a larger error than model II because of the point-charge approximation. However, neither model could avoid larger errors in the case of the anisotropic shielding constants in comparison to those of conventional calculations. In fact, it is more difficult to evaluate anisotropic values than isotropic ones. Stikoff and

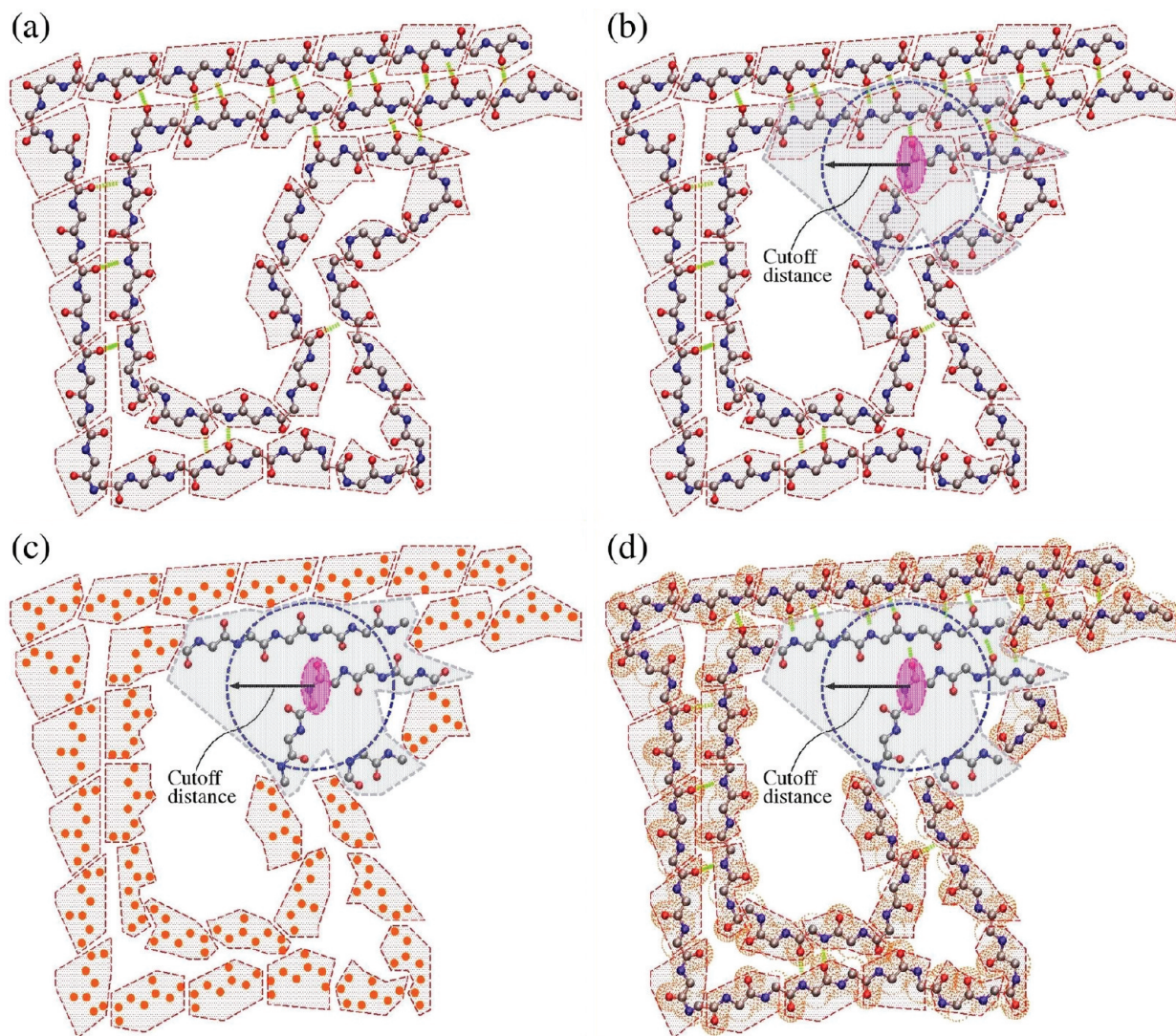


**Figure 1.** Schematics of models I and II. The procedure of the calculation of models I and II consisting of three steps. Model I, step I (a): FMO1 calculations are performed (the backbone of a peptide is shown as an example). Each fragment consists of two residues, which is indicated by the gray area surrounded by a red dashed line. Step II (b): A cutoff distance (circled by the blue dashed line), measured from the center of mass of the target residue (indicated by pink oval), is used to build a merged fragment (enclosed by the silver dashed line). Step III (c): The merged fragment in the field of point charges given by FMO1 is calculated. Step III: NMR calculation of the merged fragment is performed using the density matrix from step II. Only chemical shifts of the target residue (pink oval) are retained. The NMR results for the entire molecule are obtained by repeating steps II and III for each residue. Model II, steps I and III are the same as for model I. Instead of step II (c) in model I, the merged fragment is calculated in the external Coulomb field determined by fragment densities from FMO1 (step II (d)), shown by schematic lobes.

Case<sup>47</sup> have already mentioned this difficulty; in particular, they stated that electrostatic effects (such as electrostatic polarization of bonds and noncovalent bond interactions) and magnetic susceptibilities (such as ring-current effects) of neighboring groups are the main reasons for the deviation in the nuclear magnetic shielding tensor.

In the following, we present a method by introducing a cutoff distance to determine the optimal fragment size in models I and II to achieve an accurate description of the electrostatic effects and magnetic susceptibilities. A schematic explanation of the new NMR computational method is shown in Figure 1. The point charges and the density matrix of each fragment (monomer) are first obtained by FMO-monomer (called FMO1) calculations (Figure 1a). A merged fragment is then constructed by assembling all the

monomers within a cutoff distance (defined as  $L_{\text{cutoff}}$ ) from the center of mass (denoted by  $\mathbf{R}_a$ ) of the residue under investigation (Figure 1b). Distance  $R_{la}$  between given monomer  $I$  and examined residue  $a$  is chosen as the closest distance between atoms in  $I$  and the center of mass of  $a$  as follows:

$$R_{la} = \min_{i \in I} \{ |\mathbf{R}_i - \mathbf{R}_a| \} \quad (11)$$

where  $\mathbf{R}_i$  is the position of the  $i$ th atom in the  $I$ th monomer. A merged fragment (denoted as  $Q(L_{\text{cutoff}})$ ) including all the monomers within a given distance (eq 11) from residue  $a$  is then created. In other words, if at least one of the atoms of the monomer is inside the area  $R_{la} \leq L_{\text{cutoff}}$ , that monomer is assigned to the merged fragment,  $Q(L_{\text{cutoff}})$ . The ESP,

$V_{\mu\nu}^{Q(L_{\text{cutoff}})}$ , of fragment  $Q(L_{\text{cutoff}})$  in models I (eq 12) and II (eq 13) is expressed as

$$V_{\mu\nu}^{Q(L_{\text{cutoff}})} = \sum_{K \notin Q(L_{\text{cutoff}})} \left\{ \sum_{A \in K} \left\langle \mu \left| -\frac{1}{4\pi\epsilon_0} \frac{Z_A e^2}{|\mathbf{r} - \mathbf{R}_A|} \right| \nu \right\rangle + \sum_{A \in K} \left\langle \mu \left| \frac{1}{4\pi\epsilon_0} \frac{Z_A^K e^2}{|\mathbf{r} - \mathbf{R}_A|} \right| \nu \right\rangle \right\} \quad (12)$$

$$V_{\mu\nu}^{Q(L_{\text{cutoff}})} = \sum_{K \notin Q(L_{\text{cutoff}})} \left\{ \sum_{A \in K} \left\langle \mu \left| -\frac{1}{4\pi\epsilon_0} \frac{Z_A e^2}{|\mathbf{r} - \mathbf{R}_A|} \right| \nu \right\rangle + \sum_{\rho\sigma \in K} D_{\rho\sigma}^K (\mu\nu|\rho\sigma) \right\} \quad (13)$$

where  $Z_A^K$  is the atomic population of atom  $A$  on the  $K$ th monomer. (See also Figure 1c and d for models I and II, respectively.) Subsequently, the Fock matrix of  $Q(L_{\text{cutoff}})$  is evaluated using the ESP in eqs 12 and 13.

$$\tilde{\mathbf{F}}^{Q(L_{\text{cutoff}})} = \tilde{\mathbf{H}}^{Q(L_{\text{cutoff}})} + \mathbf{G}^{Q(L_{\text{cutoff}})} \quad (14)$$

$$\tilde{H}_{\mu\nu}^{Q(L_{\text{cutoff}})} = H_{\mu\nu}^{Q(L_{\text{cutoff}})} + V_{\mu\nu}^{Q(L_{\text{cutoff}})} + \gamma \sum_{i \in Q(L_{\text{cutoff}})} P_{\mu\nu}^i \quad (15)$$

Finally, to obtain magnetic shielding tensors, the Fock matrix is used to solve the CPHF equations. Here, the new cutoff-distance-based method is denoted as “FMO1(merged)” (where “merged” stands for the use of a merged fragment), whereas the dimer-based method in the previous work<sup>38</sup> is denoted as “FMO1(dimer).”

### 3. Computational Details

**3.1. Structural Modeling of Polypeptides.** The  $\alpha$ -helix and  $\beta$ -sheet, which are the two basic secondary structural elements in proteins, were selected to evaluate the performance of the FMO1(merged) method. An  $\alpha$ -helix peptide was chosen from one of the  $\alpha$ -helices (residues 241 to 272 of chain A) in bovine rhodopsin (Protein Data Bank code: 1HZX<sup>48</sup>). This  $\alpha$ -helix structure is stabilized by the hydrogen bonds in its main chain (Figure 2). The  $\beta$ -sheet peptide was extracted from residues 198 to 229 in the green fluorescent protein (PDB code: 1Q4B<sup>49</sup>). The  $\beta$ -sheet structure is formed from two  $\beta$ -strands, which are connected by a loop structure. As shown in Figure 2, the  $\beta$ -sheet has a more extended structure than the  $\alpha$ -helix.

Hydrogen atoms were added to both the  $\alpha$ -helix and  $\beta$ -sheet in a pH = 7 environment by using the leap module in Amber 8.<sup>50</sup> These two structures were minimized with the steepest decent and conjugated gradient methods for 2500 steps by using the Amber99 force field.<sup>51</sup> After that, MOZYME<sup>52</sup> with the AM1<sup>53</sup> Hamiltonian in MOPAC2007<sup>54</sup> was used to optimize these two peptides with a threshold value of 10 Å in the NDDO approximation. The same  $\beta$ -sheet structure was employed in ref 40, where the accuracy of the chemical shifts calculated by FMO1(dimer)/model I and FMO1(dimer)/model II was assessed.

**3.2. FMO1(merged) Calculations.** The computational process for FMO1(merged)/model I and FMO1(merged)/

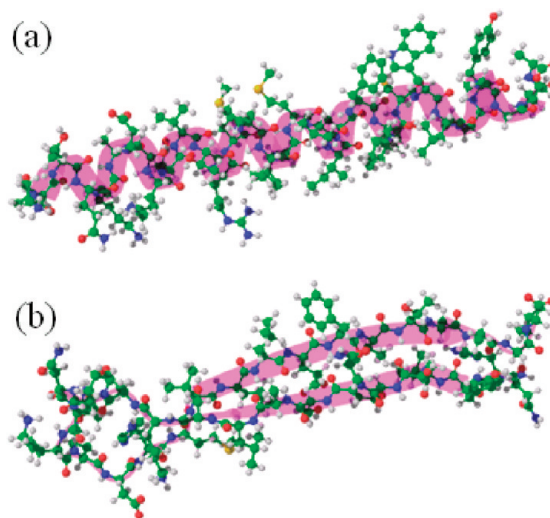


**Figure 2.** (a)  $\alpha$ -Helix and (b)  $\beta$ -sheet polypeptide structures used for calculating NMR chemical shifts in this study. Peptide sequence of the  $\alpha$ -helix is Ala-Thr-Thr-Gln-Lys-Ala-Glu-Lys-Glu-Val-Thr-Arg-Met-Val-Ile-Met-Val-Ile-Ala-Phe-Leu-Ile-Cys-Trp-Leu-Pro-Tyr-Ala-Gly-Val-Ala. Peptide sequence of the  $\beta$ -sheet is Asn-His-Tyr-Leu-Ser-Thr-Gln-Ser-Ala-Leu-Ser-Lys-Asp-Pro-Asn-Glu-Lys-Arg-Asp-His-Met-Val-Leu-Leu-Glu-Phe-Val-Thr-Ala-Ala-Gly-Ile.

model II consists of three steps. It is explained in regard to model I as follows. Step I: The polypeptide is divided into several fragments (monomers) by assigning two adjacent residues to one fragment. The electron density of all monomers is computed by performing an FMO calculation at the monomer level (FMO1 calculations). The point charges of all atoms are estimated by using the Mulliken approximation.<sup>55</sup> Step II: For each residue,  $Q(L_{\text{cutoff}})$  is determined by using  $L_{\text{cutoff}}$ . Using the ESP of eq 12, the wave function of  $Q(L_{\text{cutoff}})$  is obtained. Step III: Using the wave function obtained in step II, CPHF calculations are performed with GIAO or CSGT methods to determine the NMR magnetic shielding tensors of  $Q(L_{\text{cutoff}})$ .

In regard to model II, steps I and III are the same as for model I. The difference from model I appears in step II. According to eq 13, the monomer density matrices are used to evaluate the ESP outside  $L_{\text{cutoff}}$ . The CSGT method is used for model II (see section 2.3).

To obtain the NMR shielding tensors of the polypeptide, steps II and III are performed for all the residues. The isotropic and anisotropic shielding constants are evaluated from the shielding tensors. The anisotropic shielding constant is defined as

$$\Delta\sigma = \sigma_3 - (\sigma_1 + \sigma_2)/2 \quad (16)$$

where  $\sigma_1$ ,  $\sigma_2$ , and  $\sigma_3$  are the eigenvalues of nuclear magnetic shielding tensor  $\sigma$ , and  $\sigma_3$  is the largest of these.

The dependence of shielding constants on  $L_{\text{cutoff}}$  (6, 8, and 10 Å) used in FMO1(merged)/model I and FMO1(merged)/model II is investigated. For comparison, the shielding constants calculated without the  $V_{\mu\nu}^{Q(L_{\text{cutoff}})}$  term, that is, the shielding constants of the merged molecule surrounded by neither point charges nor the ESP of other fragments, are shown. Further-

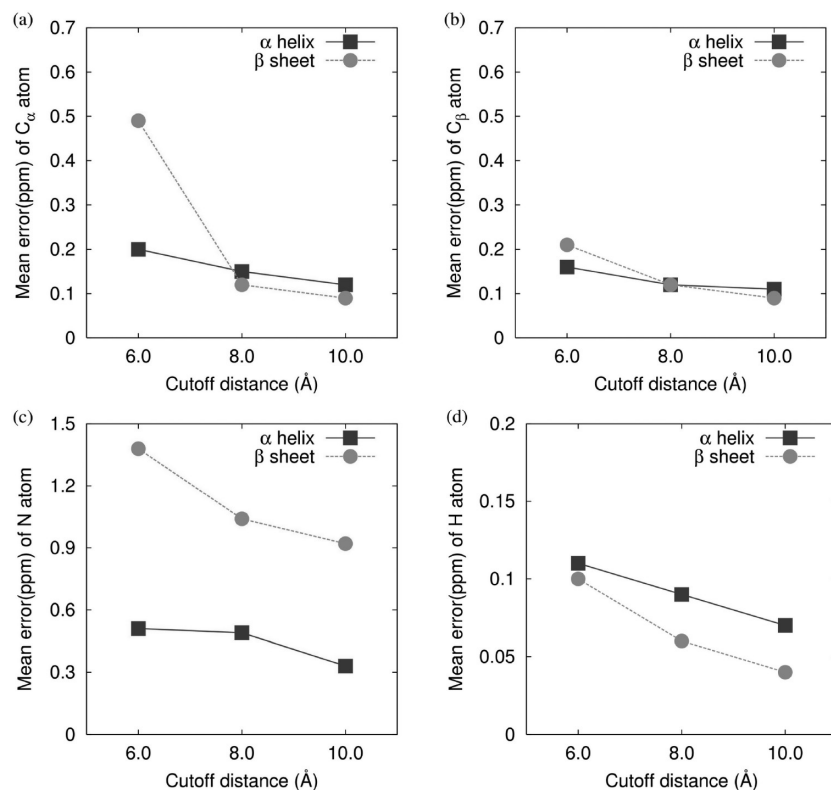


**Figure 3.** Mean error of isotropic shielding constants as a function of cutoff distances obtained by FMO1(merged)/model I with CSGT calculations (6-31G(d)) in the case of the  $\alpha$ -helix (solid line with squares) and the  $\beta$ -sheet (dashed line with circles). (a)  $^{13}\text{C}_{\alpha}$ , (b)  $^{13}\text{C}_{\beta}$ , (c)  $^{15}\text{N}$ , and (d)  $^1\text{H}$  atoms.

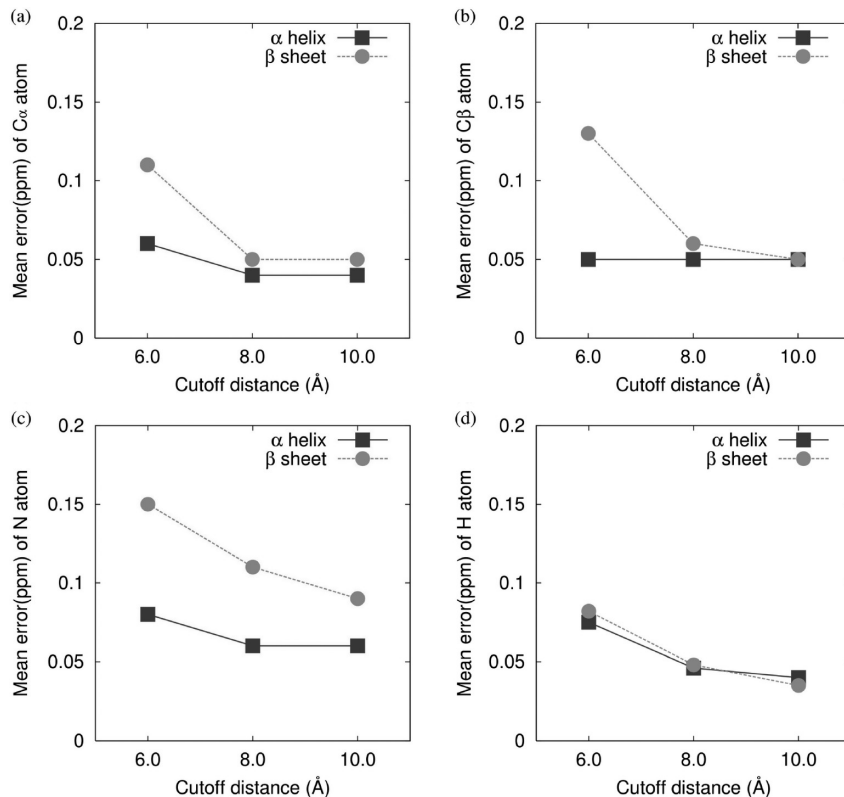


**Figure 4.** Mean error of isotropic shielding constants as a function of cutoff distances obtained by FMO1(merged)/model II with CSGT calculations (6-31G(d)) in the case of the  $\alpha$ -helix (solid line with squares) and the  $\beta$ -sheet (dashed line with circles). (a)  $^{13}\text{C}_{\alpha}$ , (b)  $^{13}\text{C}_{\beta}$ , (c)  $^{15}\text{N}$ , and (d)  $^1\text{H}$  atoms.

more, the effect of basis sets (6-31G(d) and 6-311G(d,p)) on the shielding constants was tested. The FMO and NMR (GIAO

and CSGT) calculations were performed using GAMESS<sup>56</sup> and Gaussian 03,<sup>57</sup> respectively. In the following, the errors of

**Table 1.** Quality of Absolute Isotropic NMR Shielding Constants (in ppm) of  $^{13}\text{C}_\alpha$ ,  $^{13}\text{C}_\beta$ ,  $^{15}\text{N}$ , and  $^1\text{H}$  Atoms in the  $\alpha$ -Helix and  $\beta$ -Sheet Calculated with FMO1(merged)/model I by Using CSGT and the 6-31G(d) Basis Set

atoms cutoff ( $\text{\AA}$ )	$^{13}\text{C}_\alpha$			$^{13}\text{C}_\beta$			$^{15}\text{N}$			$^1\text{H}$		
	6.0	8.0	10.0	6.0	8.0	10.0	6.0	8.0	10.0	6.0	8.0	10.0
$\alpha$ -Helix in Bovine Rhodopsin 1HZX (residues 241–272)												
max error	0.58	0.33	0.26	0.41	0.31	0.31	2.19	2.19	1.16	0.26	0.20	0.17
mean error	0.20	0.15	0.12	0.16	0.12	0.11	0.51	0.49	0.33	0.11	0.09	0.07
standard deviation	0.14	0.09	0.08	0.11	0.08	0.08	0.40	0.39	0.26	0.07	0.06	0.04
$\beta$ -Sheet in Green Fluorescent Protein 1Q4B (residues 198–229)												
max error	1.74	0.26	0.26	0.92	0.49	0.41	3.56	3.01	2.21	0.31	0.14	0.11
mean error	0.49	0.12	0.09	0.21	0.12	0.09	1.38	1.04	0.92	0.10	0.06	0.04
standard deviation	0.54	0.08	0.07	0.20	0.11	0.09	0.96	0.78	0.63	0.08	0.03	0.03

**Table 2.** Quality of Absolute Anisotropic NMR Shielding Constants (in ppm) of  $^{13}\text{C}_\alpha$ ,  $^{13}\text{C}_\beta$ ,  $^{15}\text{N}$ , and  $^1\text{H}$  Atoms in the  $\alpha$ -Helix and  $\beta$ -Sheet Calculated with FMO1(merged)/model I by Using CSGT and the 6-31G(d) Basis Set

atoms cutoff ( $\text{\AA}$ )	$^{13}\text{C}_\alpha$			$^{13}\text{C}_\beta$			$^{15}\text{N}$			$^1\text{H}$		
	6.0	8.0	10.0	6.0	8.0	10.0	6.0	8.0	10.0	6.0	8.0	10.0
$\alpha$ -Helix in Bovine Rhodopsin 1HZX (residues 241–272)												
max error	1.42	1.42	0.77	0.99	0.62	0.62	1.52	1.52	1.06	1.96	1.37	0.70
mean error	0.67	0.48	0.32	0.29	0.21	0.17	0.59	0.47	0.36	1.10	0.68	0.43
standard deviation	0.35	0.32	0.22	0.25	0.19	0.14	0.41	0.35	0.25	0.54	0.31	0.17
$\beta$ -Sheet in Green Fluorescent Protein 1Q4B (residues 198–229)												
max error	2.40	1.54	1.13	1.92	0.72	0.59	2.98	2.07	1.60	2.56	1.03	0.85
mean error	1.02	0.65	0.45	0.54	0.25	0.17	0.95	0.47	0.37	0.64	0.42	0.27
standard deviation	0.62	0.37	0.28	0.46	0.19	0.15	0.77	0.44	0.32	0.56	0.28	0.20

**Table 3.** Quality of Absolute Isotropic NMR Shielding Constants (in ppm) of  $^{13}\text{C}_\alpha$ ,  $^{13}\text{C}_\beta$ ,  $^{15}\text{N}$ , and  $^1\text{H}$  Atoms in the  $\alpha$ -Helix and  $\beta$ -Sheet Calculated with FMO1(merged)/model II by Using CSGT and the 6-31G(d) Basis Set

atoms cutoff ( $\text{\AA}$ )	$^{13}\text{C}_\alpha$			$^{13}\text{C}_\beta$			$^{15}\text{N}$			$^1\text{H}$		
	6.0	8.0	10.0	6.0	8.0	10.0	6.0	8.0	10.0	6.0	8.0	10.0
$\alpha$ -Helix in Bovine Rhodopsin 1HZX (residues 241–272)												
max error	0.18	0.12	0.12	0.13	0.13	0.10	0.24	0.20	0.20	0.15	0.09	0.08
mean error	0.06	0.04	0.04	0.05	0.05	0.05	0.08	0.06	0.06	0.08	0.05	0.04
standard deviation	0.04	0.03	0.03	0.03	0.03	0.03	0.06	0.05	0.05	0.04	0.03	0.02
$\beta$ -Sheet in Green Fluorescent Protein 1Q4B (residues 198–229)												
max error	0.26	0.15	0.15	0.48	0.16	0.15	0.68	0.24	0.24	0.29	0.11	0.09
mean error	0.11	0.05	0.05	0.13	0.06	0.05	0.15	0.11	0.09	0.08	0.05	0.04
standard deviation	0.07	0.04	0.03	0.13	0.04	0.04	0.15	0.07	0.07	0.07	0.03	0.02

**Table 4.** Quality of Absolute Anisotropic NMR Shielding Constants (in ppm) of  $^{13}\text{C}_\alpha$ ,  $^{13}\text{C}_\beta$ ,  $^{15}\text{N}$ , and  $^1\text{H}$  Atoms in the  $\alpha$ -Helix and  $\beta$ -Sheet Calculated with FMO1(merged)/model II by Using CSGT and the 6-31G(d) Basis Set

atoms cutoff ( $\text{\AA}$ )	$^{13}\text{C}_\alpha$			$^{13}\text{C}_\beta$			$^{15}\text{N}$			$^1\text{H}$		
	6.0	8.0	10.0	6.0	8.0	10.0	6.0	8.0	10.0	6.0	8.0	10.0
$\alpha$ -Helix in Bovine Rhodopsin 1HZX (residues 241–272)												
max error	0.77	0.77	0.48	0.77	0.47	0.47	0.90	0.77	0.54	1.86	1.36	0.71
mean error	0.44	0.32	0.21	0.26	0.19	0.13	0.42	0.32	0.20	1.08	0.67	0.42
standard deviation	0.20	0.15	0.11	0.18	0.14	0.11	0.25	0.21	0.15	0.53	0.30	0.18
$\beta$ -Sheet in Green Fluorescent Protein 1Q4B (residues 198–229)												
max error	2.44	1.07	0.85	1.27	0.69	0.53	1.71	0.69	0.61	2.21	0.93	0.73
mean error	1.05	0.52	0.36	0.45	0.25	0.14	0.75	0.37	0.28	0.57	0.37	0.24
standard deviation	0.60	0.26	0.21	0.33	0.16	0.13	0.47	0.19	0.15	0.49	0.24	0.18

shielding constants are reported as deviations compared to the shielding constants by conventional *ab initio* methods.

## 4. Results and Discussion

**4.1. Accuracy Comparison of FMO1(merged) and FMO1(dimer).** The errors in shielding constants using FMO1(merged) are much smaller than those obtained with the previously developed FMO1(dimer). These errors are

summarized in Tables 1–4. In the case of FMO1(merged)/model I, both the isotropic and anisotropic shielding constants of carbon atoms ( $^{13}\text{C}_\alpha$  and  $^{13}\text{C}_\beta$ ) agree well with those determined by conventional *ab initio* NMR calculations. Although FMO1(dimer)/model II gives isotropic shielding constants with a larger maximum error (less than 3.88 ppm) and mean error (less than 0.89 ppm),<sup>40</sup> FMO1(merged)/model II with CSGT ( $L_{\text{cutoff}} = 10 \text{ \AA}$ ) reduces the maximum

**Table 5.** Quality of Absolute Isotropic NMR Shielding Constants (in ppm) of  $^{13}\text{C}_\alpha$ ,  $^{13}\text{C}_\beta$ ,  $^{15}\text{N}$ , and  $^1\text{H}$  Atoms in the  $\alpha$ -Helix and  $\beta$ -Sheet Calculated with FMO1(merged) without the  $V_{\mu\nu}^Q(L_{\text{cutoff}})$  Term by Using CSGT and the 6-31G(d) Basis Set

atoms cutoff ( $\text{\AA}$ )	$^{13}\text{C}_\alpha$			$^{13}\text{C}_\beta$			$^{15}\text{N}$			$^1\text{H}$		
	6.0	8.0	10.0	6.0	8.0	10.0	6.0	8.0	10.0	6.0	8.0	10.0
$\alpha$ -Helix in Bovine Rhodopsin 1HZX (residues 241–272)												
max error	0.51	0.31	0.31	0.40	0.40	0.28	2.13	1.18	1.01	0.48	0.19	0.19
mean error	0.16	0.10	0.08	0.12	0.10	0.08	0.64	0.41	0.26	0.16	0.07	0.07
standard deviation	0.11	0.10	0.08	0.11	0.10	0.08	0.48	0.34	0.22	0.11	0.05	0.04
$\beta$ -Sheet in Green Fluorescent Protein 1Q4B (residues 198–229)												
max error	3.00	0.64	0.42	1.24	0.55	0.41	7.52	4.46	2.85	0.32	0.20	0.18
mean error	0.64	0.11	0.07	0.22	0.10	0.08	1.53	1.07	0.94	0.10	0.04	0.03
standard deviation	0.74	0.12	0.06	0.27	0.12	0.10	1.81	1.02	0.59	0.08	0.04	0.04

**Table 6.** Quality of Absolute Anisotropic NMR Shielding Constants (in ppm) of  $^{13}\text{C}_\alpha$ ,  $^{13}\text{C}_\beta$ ,  $^{15}\text{N}$ , and  $^1\text{H}$  Atoms in the  $\alpha$ -Helix and  $\beta$ -Sheet Calculated with FMO1(merged) without the  $V_{\mu\nu}^Q(L_{\text{cutoff}})$  Term by Using CSGT and the 6-31G(d) Basis Set

atoms cutoff ( $\text{\AA}$ )	$^{13}\text{C}_\alpha$			$^{13}\text{C}_\beta$			$^{15}\text{N}$			$^1\text{H}$		
	6.0	8.0	10.0	6.0	8.0	10.0	6.0	8.0	10.0	6.0	8.0	10.0
$\alpha$ -Helix in Bovine Rhodopsin 1HZX (residues 241–272)												
max error	1.33	1.17	0.71	1.00	0.60	0.58	1.00	0.75	0.78	2.04	1.40	0.79
mean error	0.64	0.37	0.31	0.31	0.21	0.16	0.40	0.31	0.30	1.16	0.70	0.44
standard deviation	0.38	0.25	0.26	0.26	0.20	0.14	0.26	0.20	0.22	0.59	0.31	0.19
$\beta$ -Sheet in Green Fluorescent Protein 1Q4B (residues 198–229)												
max error	2.24	1.24	1.04	3.42	0.81	0.68	3.13	2.27	1.74	2.67	1.02	0.86
mean error	1.00	0.55	0.40	0.76	0.34	0.20	0.92	0.48	0.33	0.65	0.41	0.27
standard deviation	0.58	0.33	0.28	0.67	0.21	0.16	0.76	0.41	0.31	0.59	0.28	0.22

and absolute mean errors of isotropic shielding constants of carbon atoms in the  $\beta$ -sheet, i.e., to less than 0.15 and 0.05 ppm, respectively, with the 6-31G(d) basis set (Table 3). And it obtains a maximum error of less than 0.85 ppm and a mean error of less than 0.36 ppm with this basis set for the anisotropic shielding constants of carbon atoms (Table 4). These errors for the anisotropic shielding constants are, again, much smaller than those with FMO1(dimer)/model II. Similarly to the case of model II, the errors for FMO1(merged)/model I (Tables 1 and 2) are much smaller than those for the FMO1(dimer)/model I calculations on  $^{13}\text{C}$  atoms.

The errors of the shielding constants for  $^{15}\text{N}$  and  $^1\text{H}$  atoms by using FMO1(merged) are remarkably reduced. For example, the maximum errors in isotropic shielding constants (determined by using FMO1 (merged)/with model II (CSGT) ( $L_{\text{cutoff}} = 10 \text{ \AA}$ ) with the 6-31G(d) basis set) of the  $\beta$ -sheet are 0.24 and 0.09 ppm for  $^{15}\text{N}$  and  $^1\text{H}$ , respectively (Table 3). In contrast, the previously reported<sup>40</sup> maximum errors in isotropic shielding constants (determined by using FMO1(dimer)/model II (CSGT) with the same basis sets) were 7.51 and 0.96 ppm for  $^{15}\text{N}$  and  $^1\text{H}$ , respectively. Because the shielding constants of these two atoms are more sensitive to the surrounding chemical environment than that of  $^{13}\text{C}$  atoms, such a large error must have been produced by the inaccuracy of the FMO1(dimer) models in reproducing the surrounding chemical environment.

These results indicate that FMO1(merged) provides a much more accurate electrostatic description and magnetic susceptibilities around the atom of interest than those provided by FMO1(dimer). This improved accuracy is discussed further in sections 4.5 to 4.8.

**4.2. Effect of Cutoff Distance.** The effect of cutoff distance on the accuracy of shielding constants is investigated in the following. This investigation focused on two questions:

First, how large should the cutoff distance be to accurately reproduce conventional *ab initio* results? Second, does the effect of cutoff distance depend on the choice of polypeptide structures?

The shielding constants of the  $\alpha$ -helix structure were calculated by using FMO1(merged)/model I with CSGT and the 6-31G(d) basis set. The calculation results are compared with the results obtained with the conventional *ab initio* method in Tables 1 and 2. For the most environmentally sensitive anisotropic shielding constants of the  $\alpha$ -helix, the larger the  $L_{\text{cutoff}}$  (from 6 to 10  $\text{\AA}$ ), the smaller the mean error. A similar trend is also found in regard to the isotropic shielding constants.

The shielding constants of the  $\beta$ -sheet were also calculated using FMO1(merged)/model I. The errors of anisotropic shielding constants for  $^1\text{H}$  atoms in the  $\beta$ -sheet are smaller than those for  $^1\text{H}$  atoms in the  $\alpha$ -helix, while those for  $^{13}\text{C}$  and  $^{15}\text{N}$  atoms in the  $\beta$ -sheet are slightly larger. A significantly larger decrease in mean error is found in the case of the  $\beta$ -sheet than in the case of the  $\alpha$ -helix when  $L_{\text{cutoff}}$  increased from 6 to 8  $\text{\AA}$  (Figure 3). In contrast, when the cutoff distance increases from 8 to 10  $\text{\AA}$ , the decrease in the mean error in the isotropic values for the  $\alpha$ -helix and  $\beta$ -sheet is almost the same. A similar decrease in error is also found for the shielding constants of  $^{13}\text{C}_\alpha$ ,  $^{13}\text{C}_\beta$ , and  $^{15}\text{N}$  atoms calculated with FMO1(merged)/model II (Figure 4). For  $^1\text{H}$  atoms, the decrease in error is almost the same from 6 to 10  $\text{\AA}$ .

We suggest that the cutoff-distance dependency of the chemical shifts is due to the secondary structures. The structure of the  $\beta$ -sheet is more extended than that of the  $\alpha$ -helix. Therefore, in regard to the total number of residues sequentially along the polypeptide (counted from the residue where the chemical shifts are calculated to the residue at

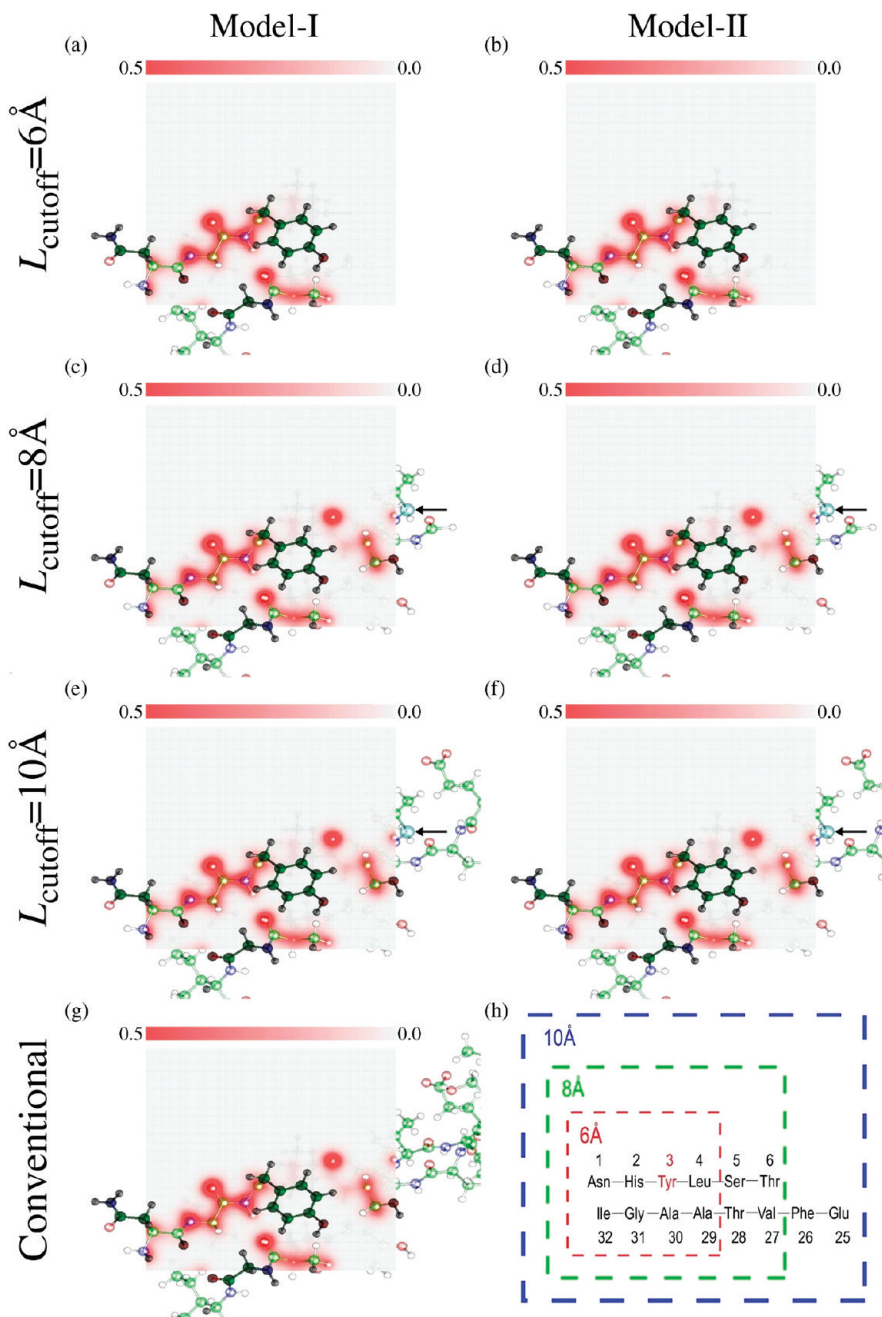


**Figure 5.** Charge density on the surface specified by three atoms (C, O, and N) of the peptide bond between His2 and Tyr3 in the  $\beta$ -sheet. The magnitude of the charge density is expressed in proportion to the intensity of the color (red), which is indicated as the gradation of the color at the top of each panel. The unit is in  $e/(a_0)^3$ , where  $a_0$  is the Bohr radius and the area is  $15.7 \times 15.7 \text{ \AA}^2$ . FMO1(merged)/model I results obtained using CSGT (6-31G(d)) with  $L_{\text{cutoff}}$  values of (a) 6  $\text{\AA}$ , (c) 8  $\text{\AA}$ , and (e) 10  $\text{\AA}$  and FMO1(merged)/model II results obtained using CSGT (6-31G(d)) with  $L_{\text{cutoff}}$  values of (b) 6  $\text{\AA}$ , (d) 8  $\text{\AA}$ , and (f) 10  $\text{\AA}$ . (g) Results of conventional *ab initio* calculation using CSGT (6-31G(d)). One of the border atoms at the fragment boundary is represented as a light-green transparent sphere and indicated by an arrow for each panel. (h) Residues within  $L_{\text{cutoff}}$  from the center of mass of Try3 are shown.

the FMO boundary), the number is larger in the  $\alpha$ -helix than in the  $\beta$ -sheet. In other words, if the same cutoff distance is used for the  $\alpha$ -helix and the  $\beta$ -sheet, the effect of the FMO boundary is larger for the  $\beta$ -sheet than for the  $\alpha$ -helix. The effect of the FMO boundary, however, is sufficiently small for the cutoff distance of 8  $\text{\AA}$ ; thus, the magnitude of errors is similar for the  $\alpha$ -helix and  $\beta$ -sheet for  $L_{\text{cutoff}} \geq 8 \text{ \AA}$ .

**4.3. Effect of Basis Sets.** To assess the dependence of the cutoff distance on the type of basis set, basis sets

6-31G(d) and 6-311G(d,p) were used. (As is well-known, a large basis set is needed to obtain accurate chemical-shift values.) The shielding constants of the  $\alpha$ -helix and  $\beta$ -sheet polypeptides, which were calculated with the 6-311G(d,p) basis set and FMO1(merged) and the conventional method, are compared (Tables S1–S4, Supporting Information). The magnitude of errors for  $L_{\text{cutoff}} = 8 \text{ \AA}$  is converged to small values irrespective of the size of the basis set. The magnitude of errors for  $L_{\text{cutoff}} = 6 \text{ \AA}$  in

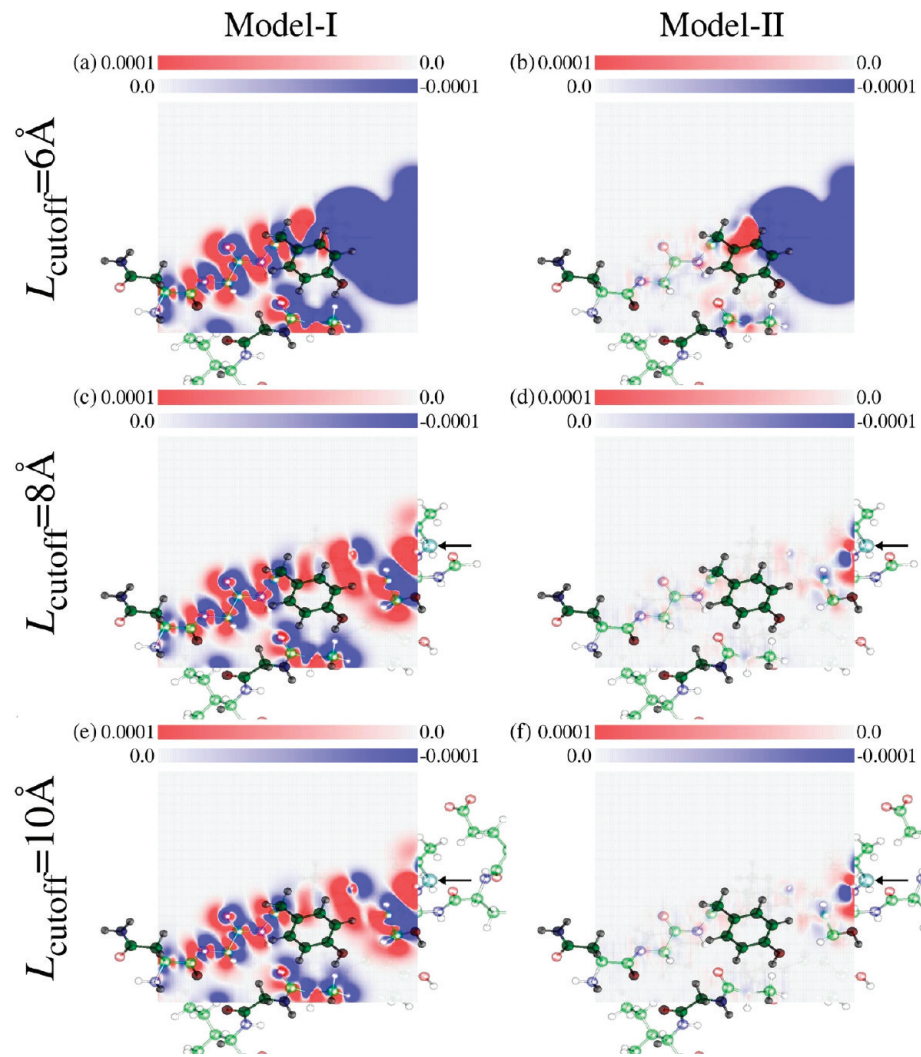


**Figure 6.** Differences between charge densities determined by FMO1(merged) and conventional *ab initio* calculations (6-31G(d)) given in Figure 5. The differences are calculated as  $\Delta\rho = \rho_{\text{FMO1(merged)}} - \rho_{\text{conventional}}$ . The magnitude of the difference in charge density is expressed in proportion to the intensity of the colors (red for positive values and blue for negative value), which are indicated as the gradation of the colors at the top of each panel. The unit is  $e/(a_0)^3$ , where  $a_0$  is the Bohr radius. Area is  $15.7 \times 15.7 \text{ \AA}^2$ . The FMO1(merged) calculation results are obtained using model I with CSGT with  $L_{\text{cutoff}}$  values of (a) 6  $\text{\AA}$ , (c) 8  $\text{\AA}$ , and (e) 10  $\text{\AA}$  and model II with CSGT with  $L_{\text{cutoff}}$  values of (b) 6  $\text{\AA}$ , (d) 8  $\text{\AA}$ , and (f) 10  $\text{\AA}$ . One of the border atoms at the fragment boundary is represented as a light-green transparent sphere and indicated by an arrow for each panel.

the case of basis set 6-311G(d,p) is larger than that in the case of basis set 6-31G(d). Accordingly,  $L_{\text{cutoff}} \geq 8 \text{ \AA}$  is recommended as the appropriate value.

**4.4. Comparison of Accuracy of Models I and II.** Model I produces a larger error than model II due to the point-charge approximation. For example, the maximum error of  $^{15}\text{N}$  isotropic shielding constants relative to the conventional *ab initio* values is 1.16–2.19 ppm with a mean error of 0.33–0.51 ppm (Table 1) in the case of the FMO1(merged)/model I calculation of the  $\alpha$ -helix with the 6-31G(d) basis set. The maximum absolute error of  $^{15}\text{N}$  isotropic shielding constants is about 300%–400% larger than the other errors of the  $^{15}\text{N}$  isotropic shielding constants for the  $\alpha$ -helix. In contrast, FMO1(merged)/model II gives shielding constants that are in excellent agreement with the conventional *ab initio* results (maximum errors, 0.20–0.24 ppm; mean errors, 0.06–0.08 ppm for  $^{15}\text{N}$  isotropic shielding constants of the  $\alpha$ -helix (Table 3)).

The accuracy of shielding constants calculated by FMO1(merged)/model I and FMO1(merged)/model II with different values of  $L_{\text{cutoff}}$  for basis set 6-31G(d) was analyzed. Model II provides much more accurate results than model I especially for isotropic values. For example, the mean error in the isotropic shielding constants of  $^{15}\text{N}$  in the  $\alpha$ -helix calculated with model II ( $\bar{\varepsilon}_{\text{Model-II}}$ ) for  $L_{\text{cutoff}} = 6 \text{ \AA}$  is significantly reduced compared to that calculated with model I ( $\bar{\varepsilon}_{\text{Model-I}}$ ) by a factor of  $\bar{\varepsilon}_{\text{Model-I}}/\bar{\varepsilon}_{\text{Model-II}} = 6.38$  (Tables 1 and 3). The larger error with model I is due to the use of Mulliken charges. This causes somewhat larger errors, especially for  $^{15}\text{N}$  and  $^1\text{H}$  atoms. The ineffectiveness of the use of Mulliken charges is clearly indicated by comparing the errors given by FMO1(merged)/model I (Tables 1 and 2) and FMO1(merged) without the  $V_{\mu\nu}^{Q(L_{\text{cutoff}})}$  term (Tables 5 and 6). The errors with FMO1(merged)/model I are similar to those with FMO1(merged) without the  $V_{\mu\nu}^{Q(L_{\text{cutoff}})}$  term. In contrast, the errors in isotropic shielding constants calculated

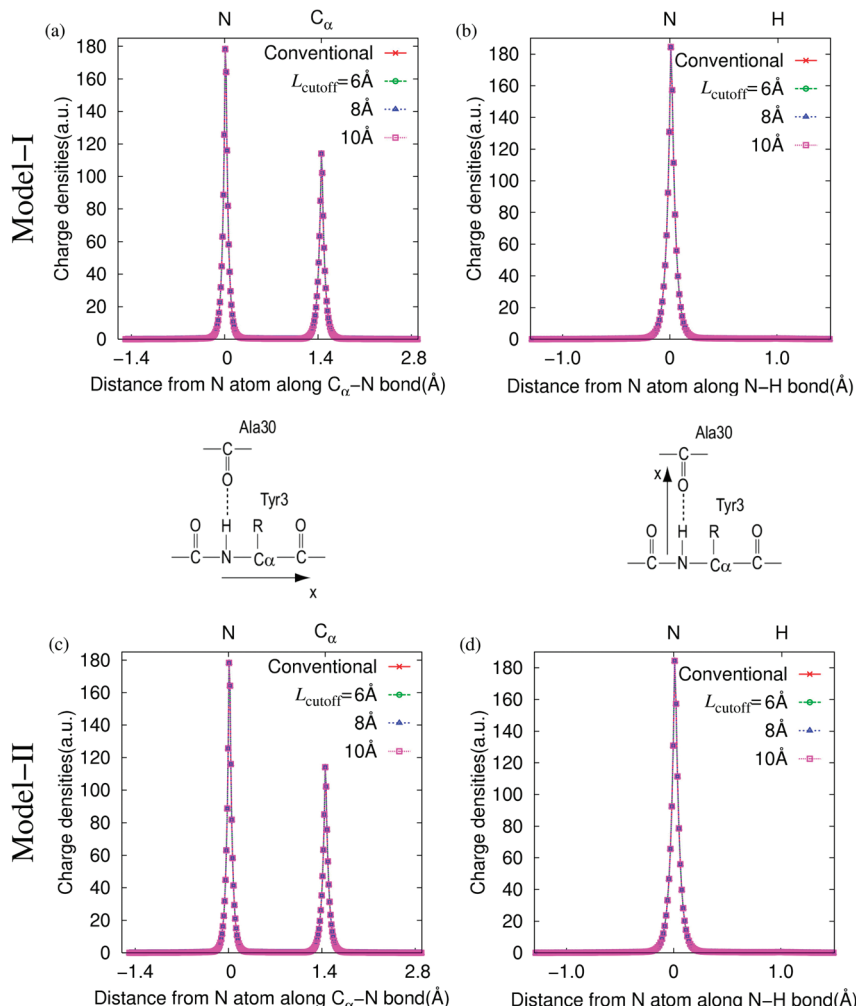


**Figure 7.** Charge densities plotted along  $C_{\alpha}$ –N and N–H bonds. Results calculated with the conventional *ab initio* method and FMO1(merged)/model I with CSGT(6-31G(d)) (a) along the  $C_{\alpha}$ –N bond and (b) along the N–H bond. Results calculated with the conventional *ab initio* method and the FMO1(merged)/model II with CSGT (6-31G(d)) (c) along the  $C_{\alpha}$ –N bond and (d) along the N–H bond. Because the curves are hard to distinguish at the scale shown, the differences are shown in Figure 8.

by FMO1(dimer)/model I are smaller than those calculated by FMO1(dimer) without the  $V_{\mu\nu}^{Q(L_{\text{cutoff}})}$  term. This is due to the fact that the effect of the ESP created by the surrounding fragments is large in the FMO1(dimer) calculations but is relatively smaller in FMO1(merged) calculations at least for  $L_{\text{cutoff}} \geq 6 \text{ \AA}$ . Thus, to improve the results calculated by FMO1(merged) for large cutoff distances, the ESP due to the surrounding fragments has to be reproduced with a high degree of precision.

**4.5. Charge-Density Distribution.** To examine the electronic structures obtained by models I and II, the distribution of the charge density in the critical area was analyzed, i.e., around the Tyr3 residue in the  $\beta$ -sheet, in which the maximum error in the isotropic values of  $^{15}\text{N}$  was found (see Figure 5 and Table S9, Supporting Information).

The charge distribution calculated with FMO1(merged) on the surface specified by three atoms (C, O, and N) of the peptide bond between His2 and Tyr3 in the  $\beta$ -sheet is given in Figure 5a–f. The magnitude of the charge density is expressed in proportion to the intensity of the color (red). The charge distributions are indistinguishable from those determined by the conventional *ab initio* calculations (Figure

5g), except for the charge distributions in the areas on the right in Figure 5a and b ( $L_{\text{cutoff}} = 6 \text{ \AA}$ ).

To clarify the difference between the charge distributions calculated in the case of three  $L_{\text{cutoff}}$  values in both models, the difference in charge densities ( $\Delta\rho = \rho_{\text{FMO1(merged)}} - \rho_{\text{conventional}}$ ) is given in Figure 6. As also shown in Figure 5, the change in the distribution of charge density is due to the change in  $L_{\text{cutoff}}$  from 6 to 8  $\text{\AA}$  (Figures 6a and b for an  $L_{\text{cutoff}}$  of 6  $\text{\AA}$  and c and d for an  $L_{\text{cutoff}}$  of 8  $\text{\AA}$ ), whereas the change is small when  $L_{\text{cutoff}}$  is increased from 8 to 10  $\text{\AA}$  (Figures 6e and f). Although the difference between models I and II is not clear in Figure 5, it is obvious in Figure 6, which plots error  $\Delta\rho$ . There is a large deviation in the charge density around the heavy atoms. The deviation in the case of model I (Figure 6a, c, and e) is more complicated than that in the case of model II (Figures 6b, d, and f).

The charge distributions along the  $C_{\alpha}$ –N and N–H bonds of Tyr3 in the  $\beta$ -sheet were examined in more detail (Figure 7). The charge densities calculated with FMO1(merged)/model I and FMO1(merged)/model II are almost identical with those calculated with the conventional *ab initio* method for all cutoff distances. Moreover, the differences in charge

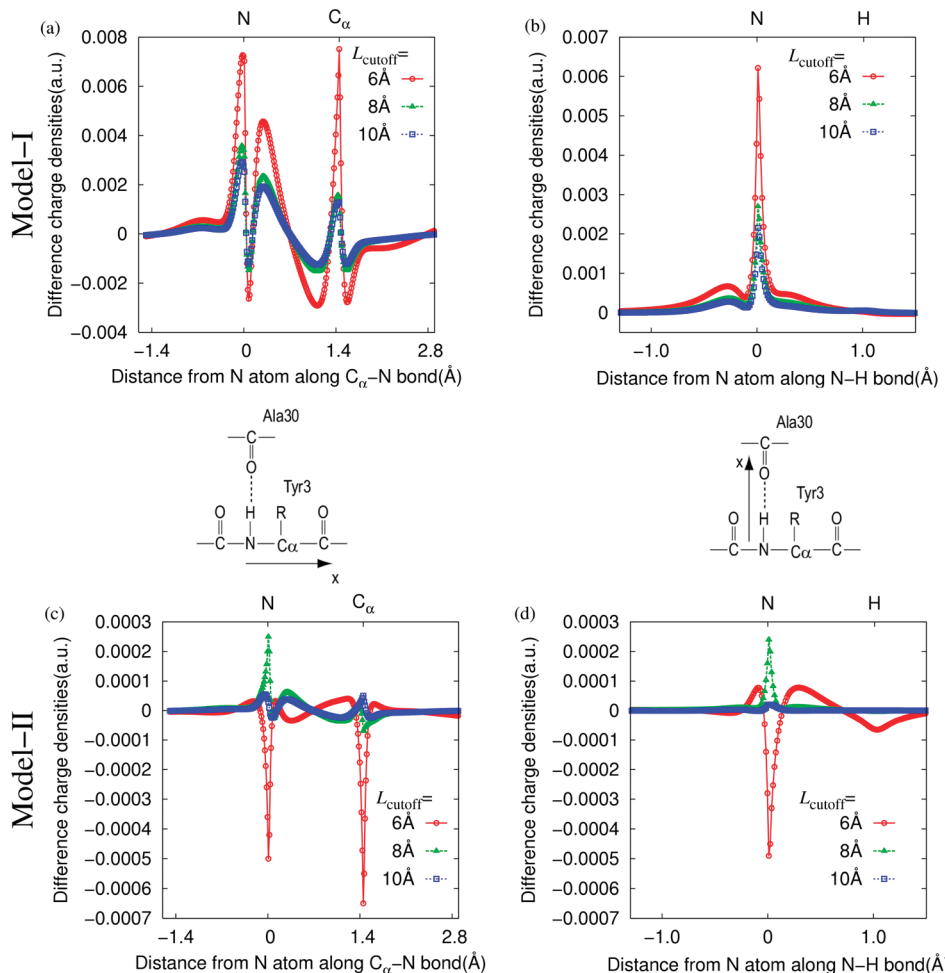


**Figure 8.** Difference between charge densities determined by FMO1(merged) and conventional *ab initio* calculations with CSGT (6-31G(d)) ( $\Delta\rho = \rho_{\text{FMO1(merged)}} - \rho_{\text{conventional}}$ ).  $\Delta\rho$  of model I (a) along the  $C_\alpha$ -N bond and (b) along the N-H bond.  $\Delta\rho$  of model II (c) along the  $C_\alpha$ -N bond and (d) along the N-H bond.

density,  $\Delta\rho$ , at  $L_{\text{cutoff}} = 6, 8$ , and  $10\text{\AA}$  for  $C_\alpha$ -N and N-H bonds (shown in Figure 8) determined by FMO1(merged) (both models I and II) and conventional *ab initio* calculations are also in excellent agreement. (Note that the scale of the vertical axis in Figure 8 is much smaller than that in Figure 7.) However, it is worth noting that the cutoff-distance dependence of charge distribution is significantly different in the cases of models I and II. The charge distribution calculated with model I strongly depends on  $L_{\text{cutoff}}$ . Increasing  $L_{\text{cutoff}}$  from 6 to 8  $\text{\AA}$  substantially improves the descriptions of the charge densities of  $C_\alpha$  and N atoms, whereas the improvement is relatively small with increasing  $L_{\text{cutoff}}$  from 8 to 10  $\text{\AA}$ . In contrast, the distribution of charge density with model II is almost independent of  $L_{\text{cutoff}}$  from 6 to 10  $\text{\AA}$ . This result indicates that a small  $L_{\text{cutoff}}$  is good enough to reproduce the charge-density distribution in the case of model II. This is because the potential used in model II is calculated from the more realistic density distributions instead of point charges used in model I.

**4.6. Electrostatic Potential.** The charge-density distribution is mainly determined by ESP. The dependence of ESP on the value of  $L_{\text{cutoff}}$  was therefore assessed. Around Tyr3, the ESP obtained with FMO1(merged) (Figure 9a-f) is compared to that obtained with conventional *ab initio* calculations (Figure 9g). It is clear that ESP is well

reproduced in the proximity of Tyr3. However, large differences in ESP determined by FMO1(merged) and the conventional *ab initio* method are found in the right-hand region far from Tyr3 for  $L_{\text{cutoff}} = 6\text{\AA}$  (Figure 9a and b). The ESP is greatly improved around the middle part on the right as the  $L_{\text{cutoff}}$  increases from 6 to 8  $\text{\AA}$  (Figure 9c and d). The ESP for  $L_{\text{cutoff}} = 10\text{\AA}$  (Figure 9e and f) is almost indistinguishable from that for conventional *ab initio* calculations (Figure 9g). Moreover, the differences between model I (Figures 9a, c, and e) and model II (Figures 9b, d, and f) are not obvious.

The differences in ESP ( $\Delta V = V_{\text{FMO1(merged)}} - V_{\text{conventional}}$ ) along the  $C_\alpha$ -N and N-H bonds for Tyr3 in the  $\beta$ -sheet are shown in Figure 10. Similar results to those described above are obtained for the differences between ESP determined by the FMO1(merged) method and the conventional *ab initio* method (Figure S1, Supporting Information). The change in the color in the peripheral area of the polypeptide in Figure 9e and f (with increasing  $L_{\text{cutoff}}$  from 8 to 10  $\text{\AA}$ ) corresponds to the change in the plateau height in Figure 10. The plateau-height change is due to the neutrality of the system with  $L_{\text{cutoff}} = 10\text{\AA}$ ; i.e., the systems with  $L_{\text{cutoff}} = 6$  or  $8\text{\AA}$  have a positive charge due to the existence of His2 (see Figure 5h), while the system with  $L_{\text{cutoff}} = 10\text{\AA}$  is neutral because of the existence of Glu25. The plateau-height

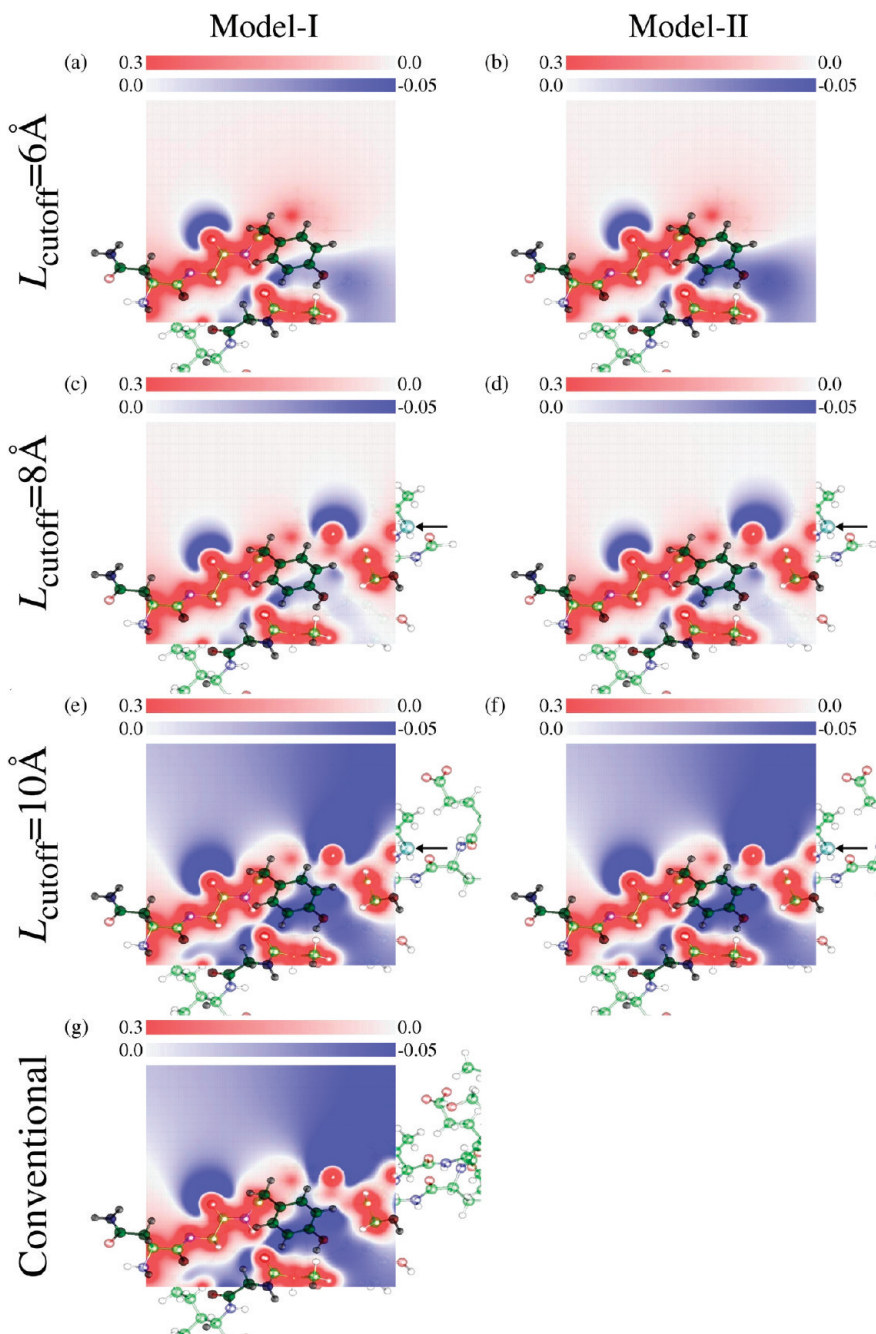


**Figure 9.** Electrostatic potential on the surface specified by three atoms (C, O, and N) of the peptide bond between His2 and Tyr3 in the  $\beta$ -sheet ( $15.7 \times 15.7 \text{ \AA}^2$ ). The magnitude of the ESP is expressed in proportion to the intensity of the colors (red for positive values and blue for negative values), which are indicated as the gradation of the colors at the top of each panel. The unit is  $e/(a_0)^3$  where  $a_0$  is the Bohr radius. All ESP values are in atomic units. FMO1(merged) results obtained using model I with CSGT (6-31G(d)) with an  $L_{\text{cutoff}}$  of (a) 6  $\text{\AA}$ , (c) 8  $\text{\AA}$ , and (e) 10  $\text{\AA}$  and model II with CSGT (6-31G(d)) with an  $L_{\text{cutoff}}$  of (b) 6  $\text{\AA}$ , (d) 8  $\text{\AA}$ , and (f) 10  $\text{\AA}$ . (g) Conventional *ab initio* calculation (6-31G(d)) results. One of the border atoms at the fragment boundary is represented as a light green transparent sphere and indicated by an arrow for each panel.

change, however, merely induces a shift in the potential near Tyr3. Consequently, the charge distribution in Figure 8 only changes slightly when  $L_{\text{cutoff}}$  increases from 8  $\text{\AA}$  and 10  $\text{\AA}$ .

**4.7. Magnetic Susceptibility.** The effects of magnetic susceptibility are considered next. Previous studies<sup>58–62</sup> using *ab initio* calculations and some empirical approaches to determine the contribution of magnetic susceptibilities to chemical shifts have revealed that this contribution mostly arises from the ring current near conjugated groups such as benzene and carbonyl bonds. These effects have a large

influence on the shielding tensor when the distance between observed atoms and the functional groups is smaller than the size of the functional groups. Accordingly, the ring-current effect was investigated by calculating the effect of the phenyl group by performing an additional calculation where a phenyl group is replaced by a hydrogen atom. (The position of the hydrogen atom is optimized by AM1.)

As shown in Figure 11, the change in the isotropic shielding constants (more than 0.1 ppm) due to the elimination of the phenyl group of Phe extends about 10  $\text{\AA}$  from

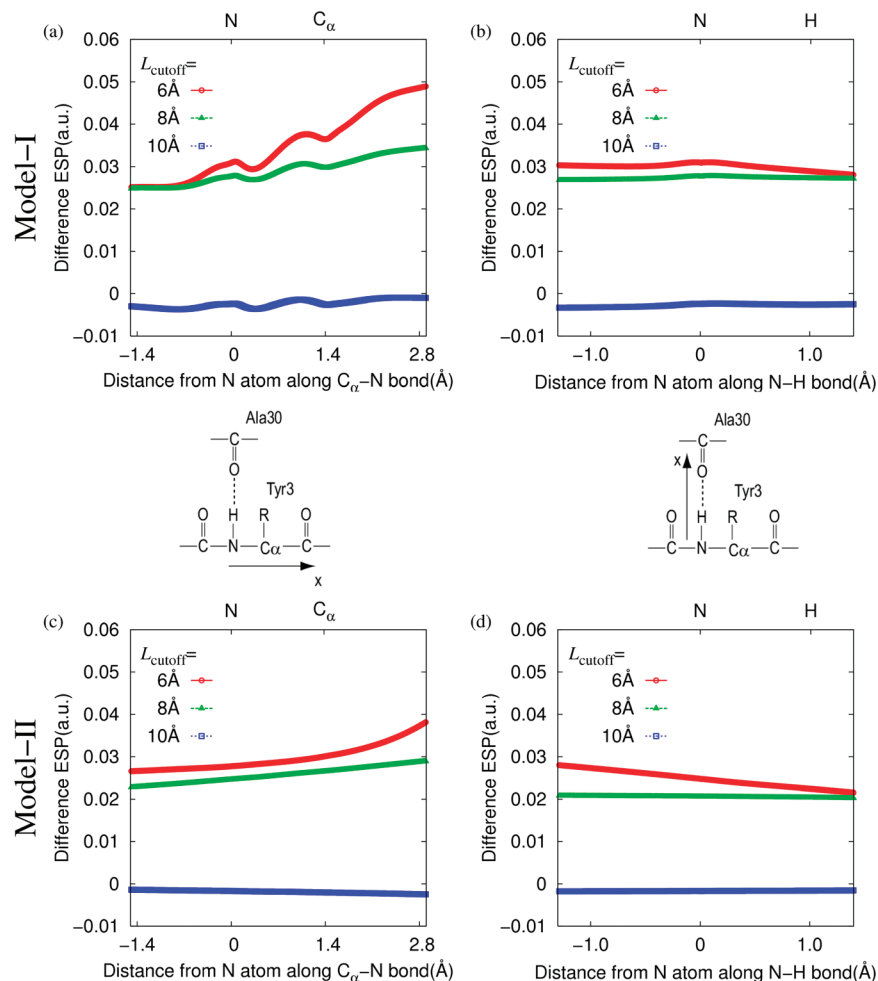


**Figure 10.** Difference between ESPs determined by FMO1(merged) and conventional *ab initio* calculations with CSGT (6-31G(d)) ( $\Delta V = V_{\text{FMO1(merged)}} - V_{\text{conventional}}$ ).  $\Delta V$  of model I (a) along the  $C_\alpha$ -N bond and (b) along the N-H bond.  $\Delta V$  of model II (c) along the  $C_\alpha$ -N bond and (d) along the N-H bond.

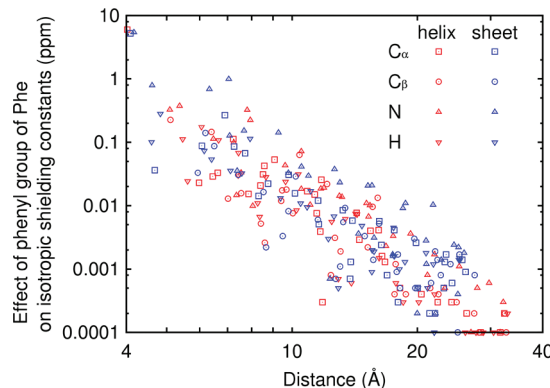


**Figure 11.** Absolute values of difference in isotropic shielding constants in the cases with or without the phenyl group of Phe in the  $\alpha$ -helix and in the  $\beta$ -sheet. Distances from the center of mass of six carbon atoms of the phenyl group to  $C_\alpha$ ,  $C_\beta$ , N, and H are shown as abscissa.

the center of the phenyl group. To confirm that the effect is not due to the difference in charge density in the cases with and without the phenyl group, the difference between the charge-density distribution with and without the phenyl group was assessed. Contours of the absolute values of the differences in electron densities in the cases with or without

the phenyl group of Phe in the  $\alpha$ -helix are shown in Figure 12. This figure indicates that the change in the charge density is localized near the phenyl group and extends over a distance of less than 10 Å. A similar result is obtained in the case of the  $\beta$ -sheet (Figure S2, Supporting Information). Thus, the difference in the isotropic shielding constants in Figure 11 at around 10 Å from the phenyl group is not due to the change in the charge density but mainly due to the ring current. Typically, a distance of about 10 Å from the phenyl group to the atoms in the backbone corresponds to an  $L_{\text{cutoff}}$  of 8 Å. Thus, an  $L_{\text{cutoff}}$  of 8 Å is an adequate distance to achieve our target accuracy of 0.1 ppm.

**4.8. FMO Boundary.** The ability to predict the electronic structure near the boundary region is discussed in the following. An artificially determined boundary may not reproduce the electronic structures accurately, considerably influencing the shielding tensor of the atoms in the vicinity of the boundary. The boundary region was thus examined by analyzing the difference between charge densities determined by the FMO1(merged) and the conventional *ab initio* method. As can be seen in Figure 6, charge densities by model I have much larger deviations in the case of conventional *ab initio* calculations compared to those obtained with model II. For example, model I (Figure 6c)

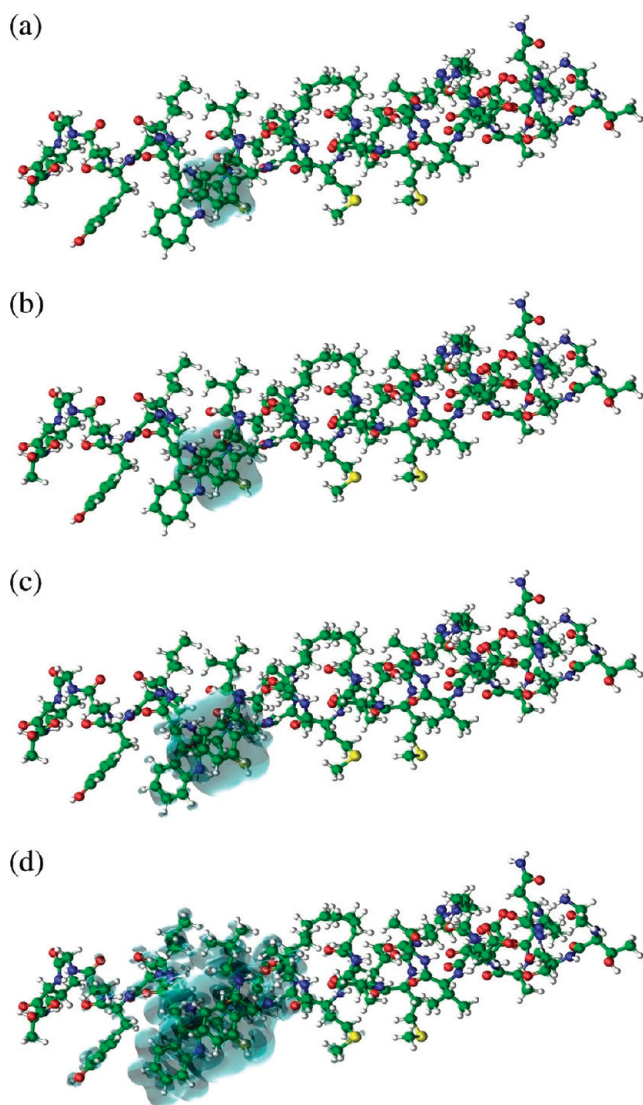


**Figure 12.** Absolute values of differences in electron densities in the cases with or without the phenyl group of Phe in the  $\alpha$ -helix. Contour values are (a) 0.01, (b) 0.001, (c) 0.0001, and (d) 0.00001  $e/(a_0)^3$ , where  $a_0$  is the Bohr radius.

shows the largest differences in charge densities around the boundary, i.e., about  $0.0044 e/(a_0)^3$ , whereas model II (Figure 6d) gives values of about  $0.0007 e/(a_0)^3$ . The large errors in charge density near the boundary in the case of model I are due to the point-charge approximation. However, because model II uses the density matrix of surrounding monomers, its quality is superior to that of model I, providing a more accurate shielding tensor.

## 5. Summary

A new *ab initio* method for calculating NMR chemical shifts—named “FMO1(merged)”—has been developed. Chemical shifts for the  $\alpha$ -helix and  $\beta$ -sheet are calculated by using the point-charge environment (referred to as model I) and the ESP of other fragments without approximation (model II). NMR shifts determined with model I agree well with those calculated by conventional *ab initio* methods (GAIO and CSGT). However, the accuracy of the chemical shifts determined by model I is

similar to that of those determined by FMO1(merged) without the  $V_{\mu\nu}^{Q(L_{\text{cutoff}})}$  term, where the ESPs of other fragments are completely neglected. Much better results were obtained with model II; that is, it provides an accurate description of the ESP and charge density around all the atoms, which results in a much better accuracy in the calculation of NMR chemical shifts. The conventional *ab initio* NMR results were reproduced using FMO1(merged)/model II with adequate cutoff distances (i.e.,  $L_{\text{cutoff}} \geq 8 \text{ \AA}$ ). This adequate value for the cutoff distance was confirmed for  $^{13}\text{C}_{\alpha}$ ,  $^{13}\text{C}_{\beta}$ ,  $^{15}\text{N}$ , and  $^1\text{H}$  atoms in  $\alpha$ -helix and  $\beta$ -sheet polypeptides with the 6-31G(d) and 6-311G(d,p) basis sets. The proposed method extends the use of the FMO method.

**Acknowledgment.** We thank Prof. M. Fujihira and Dr T. Kohno for discussion and encouragement. All the calculations were performed on the TSUBAME Grid Cluster in Tokyo Institute of Technology.

**Supporting Information Available:** Tables of results calculated with FMO1(merged)/model I and FMO1(merged)/model II by using CSGT at the 6-311G(d,p) level, FMO1(merged)/model I by using GIAO at the 6-31G(d) and 6-311G(d,p) levels, and FMO1(dimer) without the  $V_{\mu\nu}^{Q(L_{\text{cutoff}})}$  term by using CSGT at the 6-31G(d) level, a figure for the difference in ESP between FMO1(merged) and conventional *ab initio* calculations by using CSGT, a figure for the calibration of the effect of ring current. This material is available free of charge via the Internet at <http://pubs.acs.org>.

## References

- (1) Ditchfield, R. *Mol. Phys.* **1974**, *27*, 789–807.
- (2) Wolinski, K.; Hinton, J. F.; Pulay, P. *J. Am. Chem. Soc.* **1990**, *112*, 8251–8260.
- (3) Keith, T. A.; Bader, R. F. W. *Chem. Phys. Lett.* **1993**, *210*, 223–231.
- (4) One of the examples of ab initio calculations of a large peptide molecule is found in Wang, B.; Miskolzie, M.; Kotovych, G.; Pulay, P. *J. Biomol. Struct. Dyn.* **2002**, *20*, 71–79.
- (5) Warshel, A.; Karplus, M. *J. Am. Chem. Soc.* **1972**, *94*, 5612–5625.
- (6) Warshel, A.; Levitt, M. *J. Mol. Biol.* **1976**, *103*, 227–249.
- (7) Cui, Q.; Karplus, M. *J. Phys. Chem. B* **2000**, *104*, 3721–3743.
- (8) Ishida, T. *Biochemistry* **2006**, *45*, 5413–5420.
- (9) He, X.; Wang, B.; Merz, K. M. *J. Phys. Chem. B* **2009**, *113*, 10380–10388.
- (10) Sebastiani, D.; Rothlisberger, U. *J. Phys. Chem. B* **2004**, *108*, 2807–2815.
- (11) Komin, S.; Gossens, C.; Tavernelli, I.; Rothlisberger, U.; Sebastiani, D. *J. Phys. Chem. B* **2007**, *111*, 5225–5232.
- (12) Röhrig, U. F.; Sebastiani, D. *J. Phys. Chem. B* **2008**, *112*, 1267–1274.
- (13) Field, M. J.; Bash, P. A.; Karplus, M. *J. Comput. Chem.* **1990**, *11*, 700–733.
- (14) Gascón, J. A.; Sproviero, E. M.; Batista, V. S. *J. Chem. Theory Comput.* **2005**, *1*, 674–685.

- (15) Gascón, J. A.; Sproviero, E. M.; Batista, V. S. *Acc. Chem. Res.* **2006**, *39*, 184–193.
- (16) Svensson, M.; Humbel, S.; Froese, R. D. J.; Matsubara, T.; Sieber, S.; Morokuma, K. *J. Phys. Chem.* **1996**, *100*, 19357–19363.
- (17) Hall, K. F.; Vreven, T.; Frisch, M. J.; Bearpark, M. J. *J. Mol. Biol.* **2008**, *383*, 106–121.
- (18) Hua, W.; Fang, T.; Li, W.; Yu, J.-G.; Li, S. *J. Phys. Chem. A* **2008**, *112*, 10864–10872.
- (19) Rahalkar, A. P.; Ganesh, V.; Gadre, S. R. *J. Chem. Phys.* **2008**, *129*, 234101.
- (20) He, J.; Di Paola, C.; Kantorovich, L. *J. Chem. Phys.* **2009**, *130*, 144104.
- (21) Söderhjelm, P.; Ryde, U. *J. Phys. Chem. A* **2009**, *113*, 617–627.
- (22) Xie, W.; Orozco, M.; Truhlar, D. G.; Gao, J. *J. Chem. Theory Comput.* **2009**, *5*, 459–467.
- (23) Leverentz, H. R.; Truhlar, D. G. *J. Chem. Theory Comput.* **2009**, *5*, 1573–1584.
- (24) Suárez, E.; Díaz, N.; Suárez, D. *J. Chem. Theory Comput.* **2009**, *5*, 1667–1679.
- (25) Gordon, M. S.; Mullin, J. M.; Pruitt, S. R.; Roskop, L. B.; Slipchenko, L. V.; Boatz, J. A. *J. Phys. Chem. B* **2009**, *113*, 9646–9663.
- (26) Kitaura, K.; Ikeo, E.; Asada, T.; Nakano, T.; Uebayasi, M. *Chem. Phys. Lett.* **1999**, *313*, 701–706.
- (27) Fedorov, D. G.; Kitaura, K. *J. Chem. Phys.* **2005**, *122*, 054108.
- (28) Fedorov, D. G.; Kitaura, K. *J. Chem. Phys.* **2005**, *123*, 134103.
- (29) Fedorov, D. G.; Kitaura, K. *J. Chem. Phys.* **2004**, *121*, 2483–2490.
- (30) Fedorov, D. G.; Kitaura, K. *J. Phys. Chem. A* **2007**, *111*, 6904–6914.
- (31) Fedorov, D. G.; Kitaura, K. *The fragment molecular orbital method: practical applications to large molecular systems*; CRC Press: Boca Raton, FL, 2009.
- (32) Nakanishi, I.; Fedorov, D. G.; Kitaura, K. *Proteins: Struct., Funct., Bioinf.* **2007**, *68*, 145–158.
- (33) He, X.; Fusti-Molnar, L.; Cui, G.; Merz, K. M. *J. Phys. Chem. B* **2009**, *113*, 5290–5300.
- (34) Yoshida, T.; Fujita, T.; Chuman, H. *Curr. Comput.-Aided Drug Des.* **2009**, *5*, 38–55.
- (35) Takematsu, K.; Fukuzawa, K.; Omagari, K.; Nakajima, S.; Nakajima, K.; Mochizuki, Y.; Nakano, T.; Watanabe, H.; Tanaka, S. *J. Phys. Chem. B* **2009**, *113*, 4991–4994.
- (36) Sawada, T.; Fedorov, D. G.; Kitaura, K. *Int. J. Quantum Chem.* **2009**, *109*, 2033–2045.
- (37) Sekino, H.; Matsumura, N.; Sengoku, Y. *Comput. Lett.* **2007**, *3*, 423–430.
- (38) Gao, Q.; Yokojima, S.; Kohno, T.; Ishida, T.; Fedorov, D. G.; Kitaura, K.; Fujihira, M.; Nakamura, S. *Chem. Phys. Lett.* **2007**, *445*, 331–339.
- (39) Harris, R. K.; Becker, E. D.; Cabral de Menezes, S. M.; Goodfellow, R.; Granger, P. *Pure Appl. Chem.* **2001**, *73*, 1795–1818.
- (40) Yokojima, S.; Gao, Q.; Nakamura, S. *AIP Conf. Proc.* **2009**, *1102*, 164–167.
- (41) Harris, R. K.; Jackson, P.; Merwin, L. H.; Say, B. J.; Hägele, G. *J. Chem. Soc., Faraday Trans. I* **1988**, *84*, 3649–3672.
- (42) Schulz-Dobrick, M.; Metzroth, T.; Spiess, H. W.; Gauss, J.; Schnell, I. *ChemPhysChem* **2005**, *6*, 315–327.
- (43) Yates, J. R.; Pham, T. N.; Pickard, C. J.; Mauri, F.; Amado, A. M.; Gil, A. M.; Brown, S. P. *J. Am. Chem. Soc.* **2005**, *127*, 10216–10220.
- (44) Ochsenfeld, C.; Brown, S. P.; Schnell, I.; Gauss, J.; Spiess, H. W. *J. Am. Chem. Soc.* **2001**, *123*, 2597–2606.
- (45) Fedorov, D. G.; Kitaura, K. Theoretical development of the fragment molecular orbital (FMO) method. In *Modern Methods for Theoretical Physical Chemistry of Biopolymers*; Starikov, E. B., Lewis, J. P., Tanaka, S., Eds.; Elsevier: Amsterdam, 2006; pp 3–38.
- (46) Ishida, T.; Fedorov, D. G.; Kitaura, K. *J. Phys. Chem. B* **2006**, *110*, 1457–1463.
- (47) Sitkoff, D.; Case, D. A. *Prog. NMR Spectr.* **1998**, *32*, 165–190.
- (48) Teller, D. C.; Okada, T.; Behnke, C. A.; Palczewski, K.; Stenkamp, R. E. *Biochemistry* **2001**, *40*, 7761–7772.
- (49) Jain, R. K.; Ranganathan, R. *Proc. Natl. Acad. Sci. U.S.A.* **2004**, *101*, 111–116.
- (50) Case, D. A.; Darden, T. A.; Cheatham, T. A., III; Simmerling, C. L.; Wang, J.; Duke, R. E.; Luo, R.; Merz, K. M.; Wang, B.; Pearlman, D. A.; Crowley, M.; Brozell, S.; Tsui, V.; Gohlke, H.; Mongan, J.; Hornak, V.; Cui, G.; Beroza, P.; Schafmeister, C.; Caldwell, J. W.; Ross, W. S.; Kollman, P. A. *AMBER 8*; University of California: San Francisco, 2004.
- (51) Wang, J.; Cieplak, P.; Kollman, P. A. *J. Comput. Chem.* **2000**, *21*, 1049–1074.
- (52) Stewart, J. J. P. *Int. J. Quantum Chem.* **1996**, *58*, 133–146.
- (53) Dewar, M. J. S.; Zoebisch, E. G.; Healy, E. F.; Stewart, J. J. P. *J. Am. Chem. Soc.* **1985**, *107*, 3902–3909.
- (54) Stewart, J. J. P.; *MOPAC2007*, v. 1.0; Fujitsu Limited: Tokyo, 2007.
- (55) Mulliken, R. S. *J. Chem. Phys.* **1955**, *23*, 1833–1840.
- (56) Schmidt, M. W.; Baldridge, K. K.; Boatz, J. A.; Elbert, S. T.; Gordon, M. S.; Jensen, J.; Koseki, S.; Matsunaga, N.; Nguyen, K. A.; Su, S.; Windus, T. L.; Puis, M.; Montgomery, J. A. *J. Comput. Chem.* **1993**, *14*, 1347–1363.
- (57) Frisch, M. J.; Trucks, G. W.; Schlegel, H. B.; Scuseria, G. E.; Robb, M. A.; Cheeseman, J. R.; Montgomery, J. A.; Vreven, T., Jr.; Kudin, K. N.; Burant, J. C.; Millam, J. M.; Iyengar, S. S.; Tomasi, J.; Barone, V.; Mennucci, B.; Cossi, M.; Scalmani, G.; Rega, N.; Petersson, G. A.; Nakatsuji, H.; Hada, M.; Ehara, M.; Toyota, K.; Fukuda, R.; Hasegawa, J.; Ishida, M.; Nakajima, T.; Honda, Y.; Kitao, O.; Nakai, H.; Klene, M.; Li, X.; Knox, J. E.; Hratchian, H. P.; Cross, J. B.; Bakken, V.; Adamo, C.; Jaramillo, J.; Gomperts, R.; Stratmann, R. E.; Yazyev, O.; Austin, A. J.; Cammi, R.; Pomelli, C.; Ochterski, J. W.; Ayala, P. Y.; Morokuma, K.; Voth, G. A.; Salvador, P.; Dannenberg, J. J.; Zakrzewski, V. G.; Dapprich, S.; Daniels, A. D.; Strain, M. C.; Farkas, O.; Malick, D. K.; Rabuck, A. D.; Raghavachari, K.; Foresman, J. B.; Ortiz, J. V.; Cui, Q.; Baboul, A. G.; Clifford, S.; Cioslowski, J.; Stefanov, B. B.; Liu, G.; Liashenko, A.; Piskorz, P.; Komaromi, I.; Martin, R. L.; Fox, D. J.; Keith, T.; Al-Laham, M. A.; Peng,

- C. Y.; Nanayakkara, A.; Challacombe, M.; Gill, P. M. W.; Johnson, B.; Chen, W.; Wong, M. W.; Gonzalez, C.; Pople, J. A. *Gaussian 03*, Revision C.02; Gaussian, Inc.: Wallingford, CT, 2004.
- (58) Ösapay, K.; Case, D. A. *J. Am. Chem. Soc.* **1991**, *113*, 9436–9444.
- (59) Case, D. A. *J. Biomol. NMR* **1995**, *6*, 341–346.
- (60) Heine, T.; Corminboeuf, C.; Seifert, G. *Chem. Rev.* **2005**, *105*, 3889–3910.
- (61) Johnson, C. E.; Bovey, F. A. *J. Chem. Phys.* **1958**, *29*, 1012–1014.
- (62) Giessner-Prettre, C.; Pullman, B. *Q. Rev. Biophys.* **1987**, *20*, 113–172.

CT100006N